



Logic combination and diagnostic rule-based method for consistency assessment and its application to cross-sensor calibrated nighttime light image products

Zihao Zheng^{a,c}, Qiming Zheng^b, Zhifeng Wu^{a,c,*}, Zheng Cao^{a,c,*}, Hong Zhu^a, Yingbiao Chen^a, Benyan Jiang^d, Yingfeng Guo^a, Dong Xu^e, Francesco Marinello^f

^a School of Geography and Remote Sensing, Guangzhou University, Guangzhou 510006, China

^b Department of Geography and Resource Management, The Chinese University of Hong Kong, Hong Kong, SAR, China

^c MNR Key Laboratory for Geo-Environmental Monitoring of Great Bay Area, Shenzhen 518060, China

^d School of Architecture and Urban Planning, Guangzhou University, Guangzhou 510006, China

^e Department of Geography, National University of Singapore, Singapore

^f Department of Land, Environment, Agriculture and Forestry, University of Padova, Padova 35020, Italy

ARTICLE INFO

Editor Name: Dr. Marie Weiss

Keywords:

Nighttime light data

DMSP-OLS

VIIRS: Cross-sensor calibration

Logical rule

Intensity consistency

ABSTRACT

With observations from the Defense Meteorological Satellite Programme's Operational Line Scanning System (DMSP/OLS, 1992–2013) and the Suomi National Polar-Orbiting Partnership's Visible Infrared Imaging Radiometer Suite (NPP/VIIRS, 2012–), night-time light (NTL) imagery has become one of the most unique and widely-used data for understanding human activities due to its unique low-light detection capability and close correlation with socioeconomic development. Its capability for long-term observation has been further enhanced by the recent advancement in cross-sensor calibrated NTL products, which address the inconsistency between DMSP-OLS and VIIRS data and combine them together as extended NTL time series (ENTL). Despite the prosperity of cross-sensor calibration models, comprehensive and in-depth assessments of temporal consistency of their resulting ENTL products remain scarce or constrained at an aggregated scale. This study developed a new assessment scheme based on logical combinations and diagnosis rules for NTL intensity trends. Compared to previous schemes, the proposed scheme offers significant advantages in fine-grained, non-subjective intervention and semi-automation for NTL intensity consistency assessment, and its derived consistency profile layer of ENTL products can more effectively inform end-users in ENTL products selection of products and account for uncertainty in their analysis. Based on the assessment, we generated a standard light intensity dynamic trend layer (SNID) to illustrate the characteristics of global NTL intensity variations over the period from 1992 to 2020 and the applied this layer to validate the effectiveness and applicability of six most representative ENTL products. Our results showed that the scheme can automatically generate NTL intensity consistency features at a finer spatial scale than the previous TSOL-based method, and revealed for the first time a fact that has been neglected before, that is, there was a distinct gap in NTL intensity consistency among different ENTL products, with the percentage of well-matched units fluctuating from 52.81 % to 84.46 %. These variations were particularly evident in regions with high light intensity, rural areas, and high-latitude regions, reflecting the influence of spatial heterogeneity and calibration strategies. In summary, this study refines the detection process for the consistency profile of ENTL products, significantly enhancing their reliability in socioeconomic analysis and urban expansion research. By revealing the intensity consistency differences among various products, it provides critical guidance for users in data selection and application, helping to better address uncertainty.

* Corresponding authors.

E-mail addresses: zhengzh@gzhu.edu.cn (Z. Zheng), qmzheng@cuhk.edu.hk (Q. Zheng), zfwu@gzhu.edu.cn (Z. Wu), jnczdl@gzhu.edu.cn (Z. Cao), zhuhong@gzhu.edu.cn (H. Zhu), saupbyan206@gzhu.edu.cn (B. Jiang), guoyf@e.gzhu.edu.cn (Y. Guo), xu.dong@u.nus.edu (D. Xu), francesco.marinello@unipd.it (F. Marinello).

<https://doi.org/10.1016/j.rse.2025.114598>

Received 19 September 2024; Received in revised form 26 December 2024; Accepted 5 January 2025

Available online 9 January 2025

0034-4257/© 2025 Elsevier Inc. All rights are reserved, including those for text and data mining, AI training, and similar technologies.

1. Introduction

Satellite-based observations offer a unique vantage point for examining the dynamics of the Earth's surface. By detecting artificial light generated by human activities, night-time light (NTL) remote sensing provides a more direct approach to monitoring human footprints at local, regional, and global scales than “daytime” remote sensing. With the particular advantages of NTL in characterizing socio-economic activities and urban expansion, NTL-based applications have been largely expanded in recent years, including urban mapping (Li et al., 2018d; Zhang and Seto, 2011; Zhao et al., 2020; Yang et al., 2021; Zheng et al., 2021a), population and GDP spatialization (Klomp, 2016; Stokes and Seto, 2019; Yu et al., 2019; Chen et al., 2021; Chen et al., 2022b; Shi et al., 2022), energy consumption assessment (Cao et al., 2014; Román et al., 2019; Shi et al., 2019), disaster impacts and response assessment (Cao et al., 2013; Li et al., 2018a; Li et al., 2018c; Wang et al., 2018; Zhao et al., 2018), war impacts (Li et al., 2017; Li et al., 2018b; Zheng et al., 2022), human pressure and footprints (Ghosh et al., 2020; Mammides, 2020; Yin et al., 2021; Mu et al., 2022; Shi et al., 2023), air and light pollution assessment (Li et al., 2015; Jiang et al., 2017; Ji et al., 2019; Wang et al., 2020; Zheng et al., 2021b; Zhou et al., 2021).

Specifically, over the past 30 years, NTL data has been significantly enriched and advanced with the development of sensors. NTL satellites with higher spatial resolution (such as Luojia-1, which offers a spatial resolution of 130 m) and spectral resolution (such as SDGSAT-1 and Jilin-03, which provide RGB colour bands) are continually driving the refinement of NTL research. Although these novel and cutting-edge NTL data have invigorated night-time light remote sensing research, considering the availability and consistency of the datasets, the most widely used and representative NTL data currently remain those from the Defense Meteorological Satellite Program's Operational Linescan System (DMSP/OLS) and the Visible Infrared Imaging Radiometer Suite (VIIRS) on the Suomi National Polar-orbiting Partnership (NPP). Among them, version 4 DMSP/OLS stable NTL data with its relatively complete historical dataset (1992–2013) provides unique support for long-term socio-economic activity analyses. In contrast, the NPP/VIIRS NTL data, which have been processed via several streams to deliver composite products, such as daily, monthly and annual products contributed by the Earth Observation Group (EOG) (Elvidge et al., 2017, 2020, 2021) and the Black Marble suite from NASA offer higher radiometric and spatial resolution. This makes them particularly suitable for fine-scale NTL studies, with unique strengths especially in disaster response, public safety, and health stress research mentioned above.

With NTL-based applications continuing to expand, scholars are increasingly eager to combine data from multiple NTL sensors to conduct long-term human footprint or other topic-related studies, just as they typically do with optical remote sensing data (Mandanici and Bitelli, 2016; Claverie et al., 2018). Two major issues that must be addressed before a joint cross-sensor observational study can be formally implemented include 1) temporal incomparability adjustment of DMSP/OLS products obtained from different mission satellites, i.e., **inter-annual calibration**, which can be attributed to the lack of on-board calibration of the DMSP/OLS series of missions, the continued degradation of the sensors, and the factory sensitivity variations between the sensors of different missions (Zhang et al., 2016; Li et al., 2017); and 2) the alignment of the NTL images from DMSP/OLS and NPP/VIIRS, i.e., **cross-sensor calibration**, which is due to the fact that the sensors of DMSP/OLS and NPP/VIIRS have completely different parameters (Zhao et al., 2019; Levin et al., 2020; Yu et al., 2021; Zheng et al., 2023). More specifically, DMSP/OLS NTL products record relative radiation intensity, which is stored as a digital number ranging from 0 to 63, while NPP/VIIRS NTL products record absolute radiation intensity in nanoWatts/cm²/sr. Additionally, they have different spatial resolutions, with the DMSP/OLS NTL image resolution being 30 arc-seconds (~1000 m at the Equator), while the NPP/VIIRS NTL image resolution is 15 arc-seconds (~500 m at the Equator).

In this context, a series of models and strategies have been proposed to bridge the differences between DMSP/OLS and NPP/VIIRS products to generate NTL products with higher consistency quality. The initial breakthrough involved the inter-annual calibration of DMSP/OLS data, enabling the generation of continuous and comparable nighttime light (NTL) sequence products spanning the period from 1992 to 2013. For example, Elvidge et al. (2009) selected Sicily as a pseudo-invariant target and constructed a second-order polynomial model to achieve global-scale calibration; Wu et al. (2013) selected Puerto Rico, Mauritius, and Okinawa to build a global calibration model based on power functions; Li et al. (2013) selected Beijing to construct a linear function to calibrate the temporal NTL based on the above principle; Zhang et al. (2016) identified pseudo-invariant targets by ridgeline sampling and realized the calibration of the global NTL; Li and Zhou (2017) formulated a step-by-step calibration scheme by fully utilizing the temporally adjacent images as the calibration reference to realize the calibration of inter-annual NTL; Zheng et al. (2019b) identified pseudo-invariant pixels and thus realized the calibration of NTL by constructing pixel-scale regression coefficients; and Zhao et al. (2022) used models such as the power function, SARMRC, and SEAM to systematically correct the temporal NTL in order to generate a set of open-source CCNL dataset from 1992 to 2013.

Subsequent advancements focused on cross-sensor calibration, which involves the systematic integration of long-term NTL data from both DMSP/OLS and NPP/VIIRS (referred to as extended NTL, ENTNL), to track and analyze variations in NTL intensity. As of now, representative efforts can be broadly grouped into two categories according to the processing streams. The **first** category transformed the post-2012 NPP/VIIRS annual products into DMSP-like data with uniform DN values and spatial resolution to the DMSP/OLS products by conversion functions (models). For example, Li et al. (2017) who used power functions and Gaussian low-pass filters to implement the manipulation of VIIRS data to obtain DMSP-like data and combined it with the original DMSP/OLS data to estimate urban light dynamics between March 2011 and January 2017 for major human habitats in Syria. Similarly, Wu and Wang (2019) utilized this scheme to acquire time-series NTL imagery to track urban evolution in the Chinese region. Zheng et al. (2019a) employed the Lomb-Scargle periodogram technique, the BFAST time series decomposition algorithm to eliminate seasonal effects, noise, and unstable observations in VIIRS, and proposed a residual-corrected geographically weighted regression model (GWRc) to generate DMSP-like VIIRS data. Liang et al. (2020), instead, used quadratic equations and logarithmic functions, respectively, based on the invariant objective method to generate time-series consistent NTL products. Ma et al. (2020) converted the data with a biphasic dose response (BiDoseResp) model weighted by a weighted combination of sigmoid functions. Li et al. (2020) employed a sigmoid function to perform VIIRS to DMSP-like data conversion and provided global Harmonization NTL data from 1992 to 2021. Recently, Nechaev et al. (2021) selected residual U-net convolutional neural networks (CNNs) to generate DMSP-like NTL composited data and Li et al. (2023) integrated the previous schemes and proposed a set of inter-corrections for DMSP-OLS and NPP-VIIRS, developed and released the PCNL dataset for the period 1992–2021. The **second** category followed the exact opposite path, which converted DMSP/OLS to VIIRS-like data according to a specific model. The most representative work was from Chen et al. (2020), who employed trained autoencoder model to convert the time-series DMSP/OLS post-processed data to NPP-VIIRS-like NTL data. Benefiting from the exact opposite processing chain, the output from this procedure possesses a resolution of 500 m for the time-series NTL products for the period 2000–2023. Generally, the above-developed algorithms or ready-to-use extended NTL products provide critical data support for long time-series NTL-related applications and are widely used in many scenarios, such as economic growth estimation (Du et al., 2021; Chen et al., 2022a), urbanization intensity assessment (Li et al., 2021; Xu et al., 2021; Shi et al., 2023), human footprint inversion (Mu et al., 2022), carbon emissions (Jiang et al., 2023; Xu

et al., 2023), etc.

While programs for NTL time-series data consistency calibration (especially cross-sensor calibration) and ENTL products delivery are evolving, methods and metrics for assessing long-term sequence ENTL data consistency quality are still antiquated. As shown in the Table 1

Table 1

The methodology, time, and areas of the cross-sensor calibration model's performance evaluation.

Calibration model	Validation time	Validation area	Validation methods
Li et al. (2017)	Sept. 2012–Nov. 2014	Syria	<ul style="list-style-type: none"> Correlation analysis (R^2 and RMSE)
Wu and Wang (2019)	2012; 2013	Beijing	<ul style="list-style-type: none"> Pixel scatterplot Pearson's correlation coefficient and RMSE
Zheng et al. (2019a)	2012; 2013	Hangzhou	<ul style="list-style-type: none"> TSOL and GDP Pixel scatterplot Correlation analysis (R^2) Sum of the normalized different index (SNDI)
Chen et al. (2020)	2012; 2015; 2000–2018	Global: random pixels and cities Nation: United States, Italy, China, Brazil, South Africa, and Australia Local areas: Los Angeles; Shanghai; Cape Town	<ul style="list-style-type: none"> Pixel scatterplot Correlation analysis (R^2 and RMSE) Transect curves Histogram of pixels TSOL annual profile Visual comparisons
Liang et al. (2020)	2013	China-Pakistan Economic Corridor (CPEC)	<ul style="list-style-type: none"> Visual comparisons
Ma et al. (2020)	1992–2018; 2013	China, Beijing, Shanghai, Hangzhou	<ul style="list-style-type: none"> Correlation analysis (R^2) TSOL annual profile Visual comparisons Histogram of pixels Transect curves Histogram of pixels Visual comparisons TSOL annual profile
Li et al. (2020)	2012; 2013; 1992–2018	Global; Beijing-tianjin; Yangtze River Delta; Pearl River Delta; Chicago; Atlanta; Dallas	<ul style="list-style-type: none"> Visual comparisons TSOL annual profile
Nechaev et al. (2021)	2015	Las Vegas; Los Angeles; Moscow; Venezuela's gas flare	<ul style="list-style-type: none"> Correlation analysis (R^2) Visual comparisons Histogram of pixels Ratio of city-center brightness
Li et al. (2023)	2012; 2013; 1992–2021	Global; Beijing-Tianjin-Hebei region; New York; Damascus	<ul style="list-style-type: none"> Pixel scatterplot Correlation analysis (R^2 and RMSE) Visual comparisons Transect curves TSOL annual profile Average of the normalized difference index (ANDI)

below, the most common metrics used for calibration model performance assessment or ENTL products temporal consistency assessment in the aforementioned studies include the total sum of light intensities (TSOL) (Li and Zhou, 2017; Wu and Wang, 2019), correlation analysis metrics (e.g., R^2 and RMSE) (Li et al., 2017; Zheng et al., 2019a), pixel transects (Chen et al., 2020; Ma et al., 2020), and DN scatterplot or histogram assessment (Zhang et al., 2016; Li et al., 2020; Nechaev et al., 2021). Differences in metrics pre- and post-calibration were visualized to inspect the performance of the calibration model and the consistency quality of the ENTL product. These metrics were able to reveal the variations in the general level of data quality, which positively contributed to the model's optimization. However, in practical applications, these metrics still have some limitations and challenges as well:

1) Coarser analysis scales: existing methods primarily assess light intensity trends at larger scales (e.g., global, city or region scales), which is useful for overall trend analysis but lacks sensitivity to finer-scale changes, such as those at the pixel or sub-regional level. This limitation can obscure local variations in light intensity. For instance, different functional areas within a city (such as commercial versus residential zones) or urban-rural transition areas may exhibit significant intensity differences, which traditional large-scale analyses may fail to capture. Therefore, improving the granularity of assessments is essential for identifying diverse patterns within urbanization processes.

2) Subjective selection of evaluation metrics: The consistency evaluation metrics in current studies (e.g., TSOL and correlation coefficients) are often calculated based on specific regions selected subjectively by researchers, making it difficult to capture the full spatial heterogeneity of the study area. This approach can lead to substantial bias in areas with uneven light distribution, especially in rural or protected areas with lower light intensity. For example, the distinct differences in light density between urban and rural regions mean that validating ENTL product consistency only in high-density metropolitan areas may overlook light dynamics in rural or remote areas, reducing accuracy in applications like light pollution and ecological monitoring (Zheng et al., 2021b).

3) Insufficient capture of dynamic change trends: Existing methods often focus on static metrics, such as total light intensity (TSOL) or mean values, lacking an in-depth analysis of long-term dynamic change trends. In cases of urban expansion or intensifying light pollution, for instance, the dynamic characteristics of light intensity variations across time may be overlooked. Dynamic change trends often reflect the speed and direction of development in different areas, and this information is vital for understanding urbanization processes and assessing environmental changes. Without a mechanism to capture dynamic trends, essential characteristics of light radiation may be neglected, limiting the comprehensiveness of consistency evaluations.

Hence, the overarching goals of this study are: **1)** to develop a simple and efficient finer-scale consistency profile assessment scheme based on dynamic trends and logical decision rules; and **2)** to test the applicability of the proposed scheme by conducting evaluations on various representative ENTL products. The rest of the sections are as follows: the Data Sources section will present the selected representatives of the ENTL products that will be used in the proposed scheme; the Methodology section will describe in detail the proposed assessment scheme; the Results section will present the results and comparisons of the ENTL products consistency quality assessment; the Discussion section will provide the analysis of the characteristics of the methodology, the sources of ENTL product consistency variations, and the potential and limitations of the proposed scheme; and the final section will offer an overall conclusion.

2. Data sources

As of now, several models for NTL consistency calibration and affiliated products have been released, greatly promoting the application of NTL in various scenarios. Here, we have selected several high-

impact products for our research, given that they provide better coverage and data availability. Based on the time coverage available for these products, they can be divided into three categories: **1)** time-series NTL datasets for the period 1992–2012 (referred to as **period 1, p1**), derived from the interannual calibration post-processing of DMSP/OLS products; **2)** time-series NTL datasets for the period 2012–2020 (referred to as **period 2, p2**), derived from the post-processing of NPP/VIIRS products; and **3)** time-series NTL datasets for the period 1992–2020 (referred to as **full-period, fp**), derived from the post-processing of the cross-sensor calibration of DMSP/OLS and NPP/VIIRS. The sources and parameters of these products are given in Table 2.

In addition, there are some additional pre-processes to be clarified for the above-mentioned products in this study:

1. ZhangNTL and ZhengNTL presented detailed model calibration parameters. Therefore, we applied the model to the stable light products of “Version 4 DMSP-OLS Nighttime Lights Time Series” (<https://ngdc.noaa.gov/eog/dmsp/downloadV4composites.html>). Additionally, the negative pixel values after the calibration were reset to 0.
2. For those years with light images from two satellites, averaging was used in this paper to create annual light images.
3. For all products, we reconstructed the 30 arc-seconds unit grid and aligned the images to the grid using the nearest neighbor resampling and pixel aggregation methods (for VNP46A2 and ChenNTL) to reduce potential pixel-matching errors.
4. Masks of land-valid areas from ChenNTL were selected and applied as standard masks to all NTL products to eliminate pixels from areas such as oceans, lakes, and rivers.
5. For VNPv21, negative values were reset to 0.
6. For VNP46A2, since it contains weaker, random background noise, we reset values below $0.33 \text{ nanoW/cm}^2/\text{sr}$ to 0 after a sensitivity test. Later, annual light images were exported using median compositing on the GEE platform.

3. Methodology

3.1. General framework

While the time-series calibration currently available for ENTL products greatly improves the comparability of NTL data by aligning NTL intensity, it should be highlighted that this alignment needs to be performed not only at global and regional scales but even more so at finer unit scales, which have been neglected in previous studies. Therefore, the main purpose of this study is to construct an efficient and simple finer-scale (e.g., 30-arcseconds grid unit) assessment scheme to further improve the consistency quality assessment of the ENTL product. The core idea of the scheme is to create a standard reference of light intensity dynamic trends for the full period (e.g., 1992–2020) by

connecting the light intensity trends of two periods (e.g., period 1: 1992–2012, when DMSP/OLS data are available; period 2: 2012–2020, when NPP/VIIRS data are available) through a series of logic rules. Then, the reference layer will also be used to verify that the light intensity trends of the corresponding grid units in the ENTL products are consistent. Specifically, the proposed scheme can be divided into four steps:

- (1) Based on the time-series calibrated NTL products for period 1 (1992–2012), the light intensity trends were identified separately for each product. Instead of applying an averaging or weighting approach, we employed an intersection method to synthesize the standard light intensity dynamic trend layer (SNID) for period 1 (SNID_{period1}, abbreviated as SNID_{p1}). Specifically, only the grid cells where all NTL products exhibited consistent trends were retained. This approach ensures that the construction of SNID_{p1} is robust to potential biases introduced by individual products and minimizes the influence of outliers, as inconsistent or anomalous cells across products are naturally excluded during the intersection process.
- (2) Based on the time-series calibrated NTL products for period 2 (2012–2020), the light intensity trends were independently estimated for each product and intersected to synthesize the standard trend layer for period 2 (SNID_{period2}, abbreviated as SNID_{p2}). Notably, the construction of SNID_{p2} allows for the flexible integration of updated NTL datasets, enabling dynamic adjustments to extend the analysis period beyond 2020. This dynamic capability enhances the applicability and timeliness of the proposed approach, making it suitable for near-real-time consistency evaluations as new NTL data become available.
- (3) The SNID for period 1 and period 2 (i.e., SNID_{p1} and SNID_{p2}) were logically combined to construct a comprehensive SNID layer for the entire period from 1992 to 2020, referred to as SNID_{fp} (full-period SNID). This integration was achieved through carefully designed logical combination rules, ensuring that the resulting SNID_{fp} layer accurately reflects the consistency across both periods.
- (4) Similarly, the dynamic trend layer for light intensity across the full-period ENTL products, referred to as the ENID layer, was also computed. The SNID_{fp} layer was then applied in a logical diagnostic process to evaluate and identify the consistency characteristics within the ENTL products, ensuring that any discrepancies or alignments in light intensity trends were systematically assessed across the entire period. The flowchart of the whole program is shown in Fig. 1.

3.2. Grid unit level light intensity trend analysis

The key processing step in the entire program is the grid unit-based

Table 2
Selected representative time-series NTL products (including non-extended and extended NTL).

Calibration method	Abbreviation	Time period	Spatial resolution	Coverage	Availability	Selected period
Zhang et al. (2016)	ZhangNTL	1992–2012	~1 km	Global	Model parameters	1992–2012
Zheng et al. (2019b)	ZhengNTL	1992–2013	~1 km	Global	Model parameters	
Zhao et al. (2022)	CCNL	1992–2013	~1 km	Global	Model parameter Data products	
EOG intercalibrated data	V4calNTL	1992–2013	~1 km	Global	Model parameter Data products	2012–2020
Román et al. (2018)	VNP46A2	2012–2024	500 m	Global	Data products	
Elvidge et al. (2021)	VNPv21	2012–2022	~500 m	Global	Data products	
Li et al. (2020)	LiNTL	1992–2021	~1 km	Global	Data products	1992–2020
Ma et al. (2020)	MaNTL	1992–2020	~1 km	China	Data products	
Zhang et al. (2024)	PANDA	1984–2020	~1 km	China	Data products	
Nechaev et al. (2021)	NechaevNTL	1992–2019*	~1 km	Global	Data products	2000–2022
Li et al. (2023)	PCNL	1992–2021	~1 km	Global	Data products	
Chen et al. (2020)	ChenNTL	2000–2023	500 m	Global	Data products	

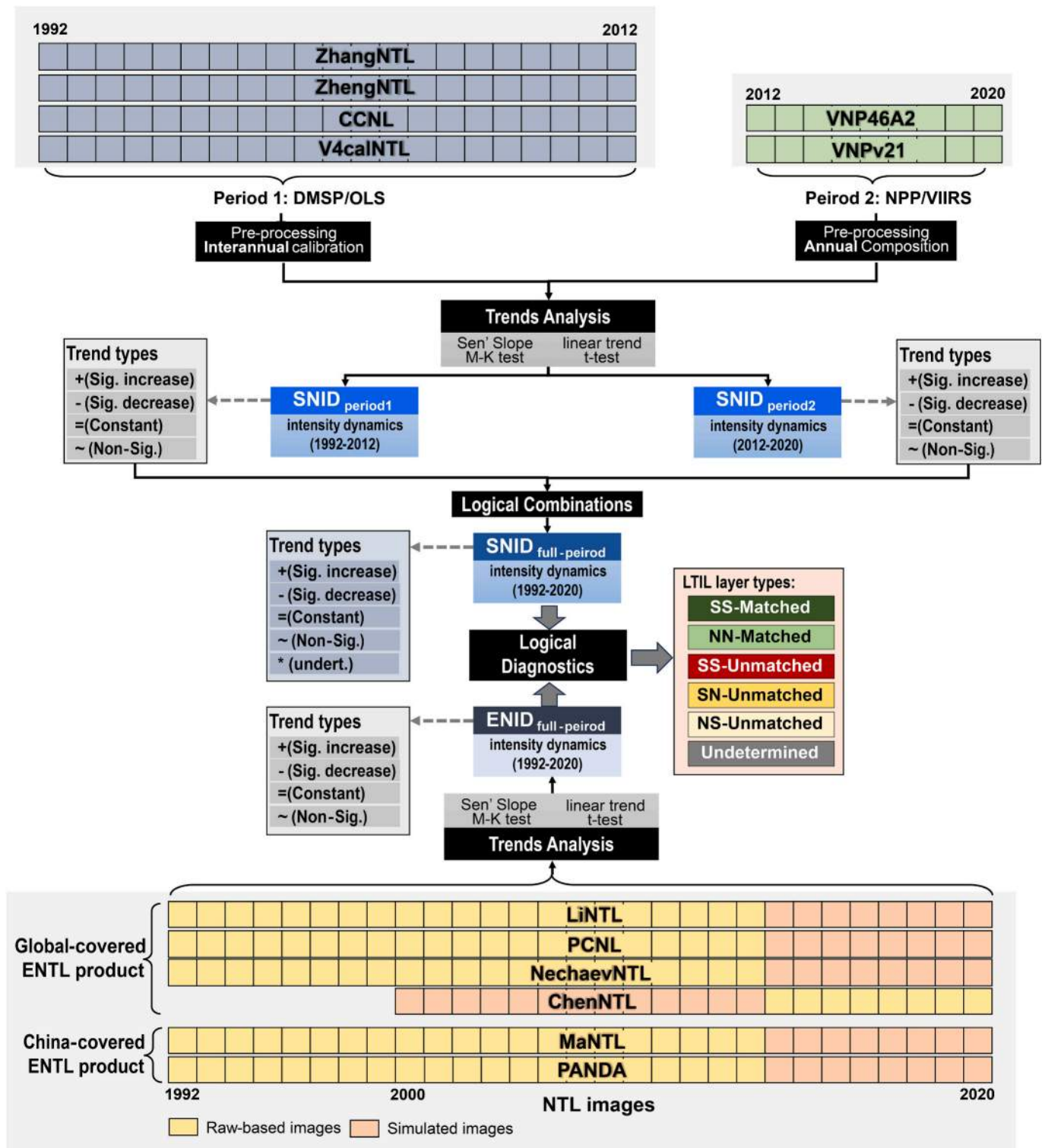


Fig. 1. Technical route for logic rule-based consistency characterization and assessment scheme for ENTL products (Note: SS-Matched = SNID_{fp} and ENID_{fp} shared a consistent and significantly trends; NN-Matched = SNID_{fp} and ENID_{fp} shared a consistent and non-significantly trends, SS-Unmatched = SNID_{fp} and ENID_{fp} showed inconsistent and significant trends, SN/NS-Unmatched = SNID_{fp} and ENID_{fp} showed mismatched significance levels).

trend analysis of light intensity. Through trend analysis and significance testing, we categorized light intensity temporal variations into the following classes: significant increase, significant decrease, no change, and no significant change-to reflect their changing patterns over the specified time profiles.

In this study, the linear trend joint *t*-test and the Mann-Kendall (M-K)

trend test were used to detect the trend of light intensity in multiple periods respectively due to their applicability and simplicity. The linear trend method, which uses ordinary least squares for parameter estimation, has been well-acknowledged for its simplicity and effectiveness, making it widely used for trend analysis of time series data (Narayanan et al., 2016). The M-K trend test, which does not require the data to

conform to a given distribution and resists data outliers, has been widely used in areas such as vegetation dynamics, precipitation detection, temperature change, and light trends (Jiang et al., 2015; Panwar et al., 2018; Xu et al., 2019).

M-K statistic S is given as:

$$S = \sum_{i=1}^{n-1} \sum_{j=i+1}^n \text{sgn}(NTL_j - NTL_i) \quad (1)$$

where NTL_j and NTL_i represent j -year and i -year pixel light DN values for NTL products, respectively and sgn is the sign function as:

$$\text{sgn}(NTL_j - NTL_i) = \begin{cases} 1 & (NTL_j - NTL_i > 0) \\ 0 & (NTL_j - NTL_i = 0) \\ -1 & (NTL_j - NTL_i < 0) \end{cases} \quad (2)$$

The variance is computed as:

$$\text{Var}(S) = \frac{n(n-1)(2n+5) - \sum_{i=1}^p t_i(t_i-1)(2t_i+5)}{18} \quad (3)$$

$$\text{Var}(S) = \frac{n(n-1)(2n+5)}{18} \quad (4)$$

where n is the length of the time series, m is the number of tied groups and t_i is the number of data value in the m th group. If there are not the tied groups, the variance can be simplified as Eq. (5). In cases where the sample size $n > 10$, the standard normal test statistic Z is computed using Eq. (6):

$$Z = \begin{cases} (S-1)/\sqrt{\text{Var}(S)} & (S > 0) \\ 0 & (S = 0) \\ (S+1)/\sqrt{\text{Var}(S)} & (S < 0) \end{cases} \quad (5)$$

where Z is the statistical value of the significance test of the time series with a value range of $(-\infty, +\infty)$. At a confidence level of $\alpha = 0.05$, $|Z| \geq Z_{0.05/2} = 1.96$ indicates that there is a significant trend in the intensity value of the unit lights.

Based on trend analysis and significance tests, the time-series light radiation variation characteristics of each pixel were identified in the following categories: 1) significant increased ($Z > 0$, $p \leq 0.05$); 2) significant decreased ($Z < 0$, $p \leq 0.05$); 3) unchanged ($Z = 0$); 4) non-significant change ($Z \neq 0$, $p > 0.05$).

3.3. Framework of logical rules

3.3.1. Logical combination rules of trends

Due to the differences in the performance parameters of the DMSP/OLS and NPP/VIIRS sensors, it is not possible to directly integrate them to carry out full-time NTL-related studies. This is the primary motivation for scholars to develop cross-sensor calibration models to produce ENTL products. However, although the units of light intensity for the NTL products from DMSP/OLS and NPP/VIIRS are completely different (one is a DN value while the other is an absolute radiation value), they are both essentially measurements of artificial light intensity characteristics on the surface at night. Despite the differences in numerical and physical units, the trend characteristics derived from them eliminate this 'gap', allowing them to be compared and joined. According to the scheme described in the previous section, based on the period 1 and period 2

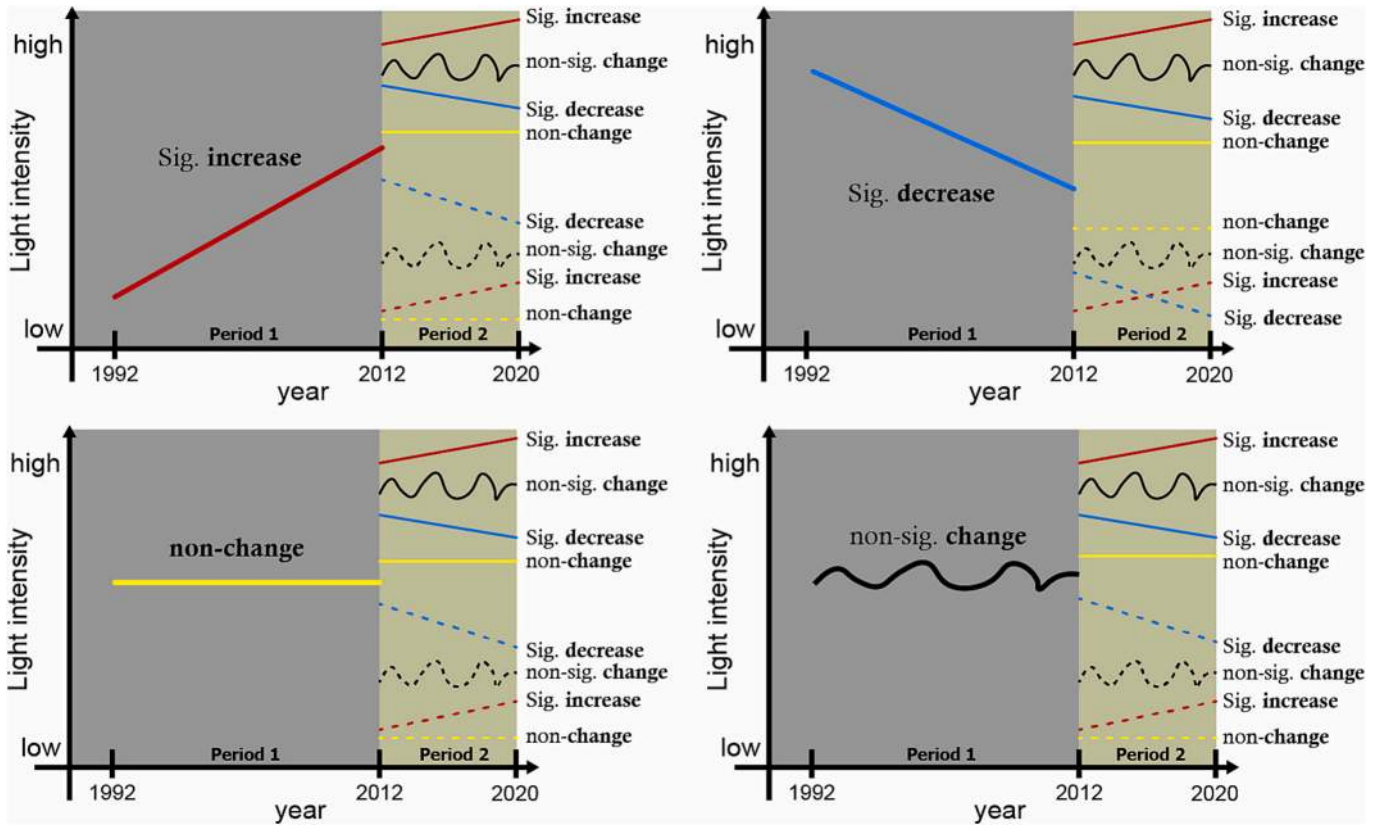


Fig. 2. Scenario case for performing the logical combinations between the period 1 and period 2 based on their trend types (Note: Period 1 and period 2 were highlighted with grey and yellow backgrounds respectively, and in each period, four types of significant increase, significant decrease, constant, and non-significant changes were identified according to the results of the trend analysis). (For interpretation of the references to colour in this figure legend, the reader is referred to the web version of this article.)

time-series NTL products, the standard light intensity dynamic trend layers for the respective periods, i.e., $SNID_{p1}$ and $SNID_{p2}$, are extracted. Then we can derive a full-period intensity trend layer, $SNID_{fp}$, by executing a series of logical combinations.

The principle of the designed logical combinations is shown in Fig. 2. The resulting combinations will lead to multiple scenarios, that is:

- If the light intensity of a particular unit significantly increased in the 1st period, then there are four possibilities of changes in the 2nd period.
- Therefore, according to their combination, Significant increase followed by Significant increase: this indicates that the light intensity significantly increased in two consecutive adjacent periods, and consequently would show a steady and significant increase over the full-period. The following is a simple mathematical proof, with linear trend analysis as an example:

Setting the actual NTL intensity as $T(x)$, x as the year and $x \in [1992, 2020]$:

Due to the sensors' performance differences, it was assumed that there is a linear relationship between the recorded values of OLS and VIIRS and the actual intensity:

$$\text{for OLS, } m(x) = \alpha_1 T(x) + \beta_1, \text{ where } \alpha_1 > 0 \text{ and } x \in [1992, 2012] \quad (6)$$

$$\text{for VIIRS, } n(x) = \alpha_2 T(x) + \beta_2, \text{ where } \alpha_2 > 0 \text{ and } x \in [2012, 2020] \quad (7)$$

Since the recorded values of both OLS and VIIRS keep a linear upward trend:

$$\text{for OLS, } m(x) = k_1 x + b_1, \text{ where } k_1 > 0 \text{ and } x \in [1992, 2012] \quad (8)$$

$$\text{for VIIRS, } n(x) = k_2 x + b_2, \text{ where } k_2 > 0 \text{ and } x \in [2012, 2020] \quad (9)$$

Thus, for $T(x)$:

$$T(x) = \frac{m(x) - \beta_1}{\alpha_1} = \frac{k_1 x + b_1 - \beta_1}{\alpha_1} \quad (10)$$

$$T(x) = \frac{n(x) - \beta_2}{\alpha_2} = \frac{k_2 x + b_2 - \beta_2}{\alpha_2} \quad (11)$$

Calculate the rate of change of T with respect to x , and since $k_1 > 0$, $\alpha_1 > 0$:

For $x \in [1992, 2012]$:

$$\frac{dT}{dx} = \frac{k_1}{\alpha_1} > 0 \quad (12)$$

For $x \in [2012, 2020]$:

$$\frac{dT}{dx} = \frac{k_2}{\alpha_2} > 0 \quad (13)$$

So, in both sub-intervals $[1992, 2012]$ and $[2012, 2020]$, $T(x)$ is a linear function of x with a positive derivative $dT/dx > 0$, and $T(x)$ is continuous at $x = 2012$ since it is a physical quantity.

Therefore, $T(x)$ is a continuous and monotonically increasing function over the entire interval which means the NTL intensity has been continuously increasing from 1992 to 2020.

For other combinations, similarly:

- Significant increase followed by significant decrease: this indicates that the dynamic trend of light intensity in two consecutive adjacent periods was completely opposite, and it is prudent to assume that the trend over the entire span was undetermined.
- Significant increase followed by constant: this means that the light intensity rises significantly in period 1 but remains constant in period 2, and for the full period, the trend would still be considered to be significantly increased.

- Significant increase followed by non-significant change: again, for caution, it was assumed that once a non-significant change occurred in a given period, their combination would still be considered a non-significant change.

Fig. 3(a) shows all the logical combination rules that generated the $SNID_{fp}$ using the $SNID_{p1}$ and $SNID_{p2}$ layers, and for easier interpretation, the trends within each period are represented by the following characters: significant increase (+), significant decrease (−), constant (=), non-significant change (~), and undetermined (*). Thus, sixteen trend combinations are established between them, and they can be further categorized into five types according to the logical rules mentioned in Fig. 2 and adopted as the standard trend layer $SNID_{fp}$ for the full-period.

3.3.2. Consistency of logical diagnostic rules

For the consistency assessment of ENTL products, it is necessary to employ the previously mentioned trend analysis for them to generate a full-period light intensity trend layer, $ENID_{fp}$, which also summarizes the time-series light change information into four types: significantly increase, significantly decrease, constant, and non-significantly change. Next, the trend layers described above will be conjoined with the standard trend layer, $SNID_{fp}$, and simple logical diagnostics will be performed. Fig. 3(b) shows the details of the logical diagnostic rules between $ENID_{fp}$ and $SNID_{fp}$. Specifically, the combination of their trend types can produce twenty combinations that are logically determined to be of six types, which are:

- Significantly matched grid units (**SS matched, SS-M**): these units were identified as significant in both $ENID_{fp}$ and $SNID_{fp}$ and have exactly the same type of change, which can be considered as units with excellent consistency in the ENTL products. It consists of three combinations: significant increase (+ +), significant decrease (− −), and constant (= =).
- Non-significantly matched grid units (**NN matched, NN-M**): these units do not show a significant trend in both $ENID_{fp}$ and $SNID_{fp}$ and thus the consistency of units of this combination (~ ~) is relatively good in the ENTL products.
- Significant unmatched grid units (**SS unmatched, SS-UM**): these units were identified as significant changes in both $ENID_{fp}$ and $SNID_{fp}$, but they have completely different trends. Therefore, units with these combinations (e.g., + −, − +) would be regarded as poor consistency units and should be concern when being applied.
- Significant non-significant unmatched grid units (**SN unmatched, SN-UM**): these units were observed as significant changes in $SNID_{fp}$ but showed non-significant changes in $ENID_{fp}$. Therefore, units with these combinations (e.g., + ~, − ~ and = ~) would be considered as having weak consistency.
- Non-significant significant unmatched grid units (**NS unmatched, NS-UM**): such units did not detect a significant trend in $SNID_{fp}$, while showing a significant change in $ENID_{fp}$. With caution, we consider these combinations (e.g., ~ +, ~ − and ~ =) as having moderate consistency.
- Undetermined grid units (**Undetermined, UD**): Since some units in $SNID_{fp}$ temporarily failed to establish their full-time trends, combinations with those trend types (e.g., * +, * −, * =, and * ~) would also be diagnosed as undetermined units.

3.4. Self-validation of the proposed scheme

The above-mentioned results showed favorable properties of simplicity, efficiency, and migration of consistency inspection of ENTL products via logical combination and diagnostic rules. However, the reliability of the program's test results still needs to be analyzed quantitatively. It must be recognized that there is still a lack of publicly available, accurate standard light trend layers that can be used as a reference, making cross-comparison options based on high-quality third-

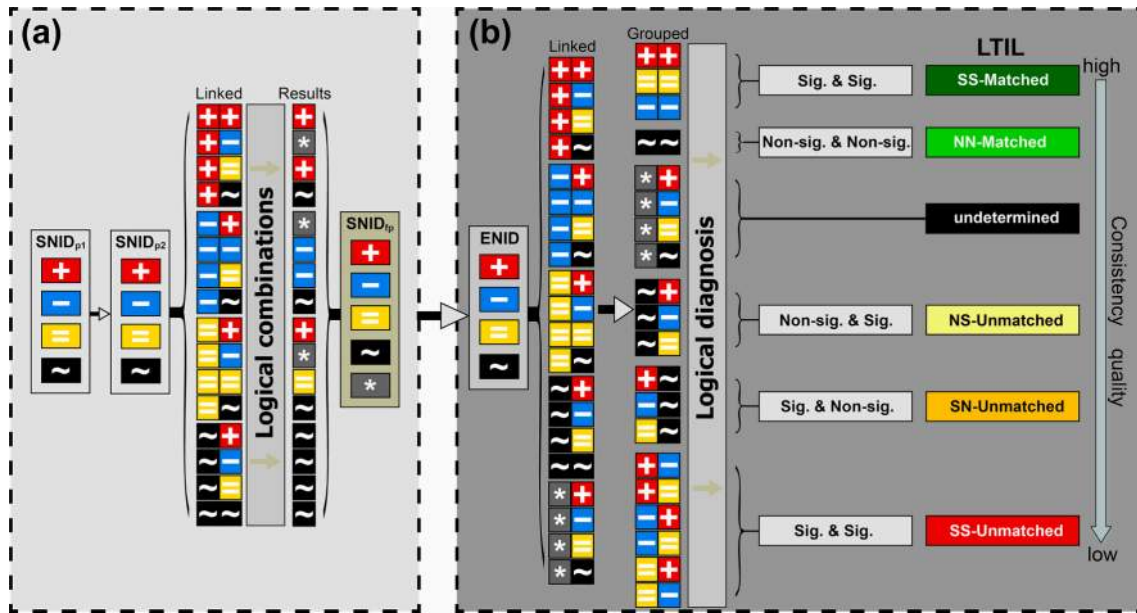


Fig. 3. (a) Logical combinations to create standard light trend layer (SNID_{fp}) and (b) performing logical diagnosis assessment to generate the ENTL products consistency characterization layer (LTIL) (Note: the symbol “~” represents non-significantly changed, the symbol “=” represents non-changed, the symbol “*” represents undetermined and the symbols “-” and “+” represent significantly decreased and increased, respectively).

party data still a big challenge. To this end, we designed a self-validation strategy, as shown in Fig. 4. Specifically:

- We generate the specific standard trend layer SNID based on ENTL’s own two separate periods through the previously designed logical combination strategy.
- Next, the specific SNID layer is utilized to logically diagnose the full-period trends of ENTL products and identify the trend matches.

Theoretically, if the logical combination and diagnostic strategies proposed in this paper are reliable, then the specific SNID layer derived from the ENTL products segmented trend combinations will have an extremely low or even negligible percentage of unmatched grid units when matched to its full period of trend, while the percentage of matched grid units will be at an extremely high level.

4. Results

4.1. Standard trend layers for period 1, period 2 and the full period

Fig. 5 shows the standard trend type maps generated for period 1 (SNID_{p1}) and period 2 (SNID_{p2}) at a 30-arcsec grid unit-scale based on the linear trend joint *t*-test and the M-K trend test, respectively. Among them, SNID_{p1} was derived from the four interannual calibration products, ZhangNTL, ZhengNTL, CCNL, and V4calNTL, by identifying the trend of period 1 separately and then exporting their intersections as the standard trend. This intersection process was necessary to imply that the type of trend identified by SNID_{p1} was sufficiently robust, as it was consistent across the four widely used interannual calibration products described above. As shown in Fig. 5(a–b), the results of the linear trend analysis showed that globally (excluding water areas) about 87.11 % of

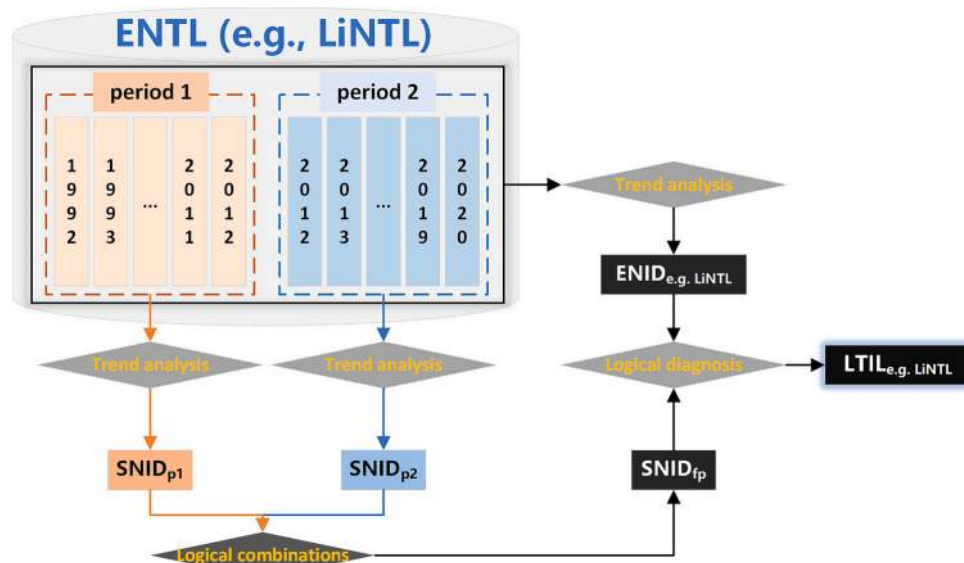


Fig. 4. The flow chart of the self-validation strategy for the proposed logic rule-based scheme.

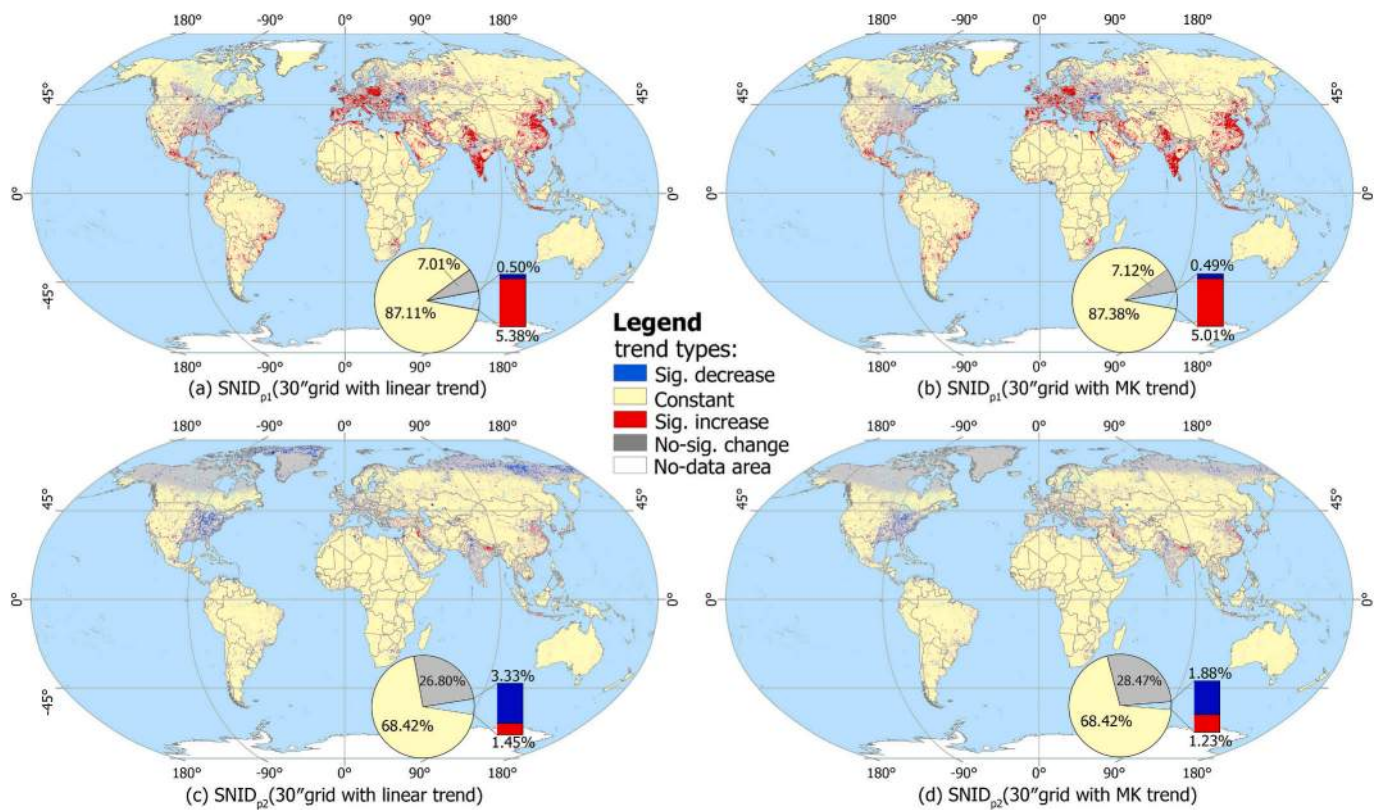


Fig. 5. Identified global light intensity trend types for period 1 and period 2 based on linear trend joint t-test and the M-K trend test.

the grid units were in a constant state during period 1, 7.01 % of the units had insignificant changes in light intensity, 5.38 % of the units had significant light increases, and 0.50 % of the units showed significant light decreases. Correspondingly, the percentage of significantly increased and significantly decreased units in the M-K trend analysis decreased slightly to 5.01 % and 0.49 %, respectively. As a precaution and to reduce the risk of overestimation, the results of the M-K trend analysis were selected to compete in the subsequent SNID_{fp} construction in this paper. In terms of the spatial distribution of significantly changed units, the results showed that the countries with a high percentage of significantly increased units were mainly in Western Europe, the Middle East, South Asia, and East Asia, while the high percentage of significantly decreased units were mainly found in Eastern Europe (Ukraine, Moldova, Slovakia), Africa (Nigeria, Libya, Algeria), and the Arabian Peninsula (Syria, Oman).

Fig. 5(c–d) indicates the results of the identification of light intensity trends for period 2. Different from SNID_{p1}, which used four representative NTL interannual calibration products for composition, SNID_{p2} was based on an annual composite image of NASA Black Marble's product VNP46A2. This is because the VNP46A2 product, one of NASA's operational Black Marble product suite (VNP46), is a nighttime light data product based on the VIIRS sensor that has passed a rigorous calibration and validation process and is representative of the high-quality NTLs that are currently accessible. The results of trend type identification showed that 68.42 % of the grid units remained constant, 28.47 % (26.80 % in linear trend) of the units showed non-significant changes, 1.23 % (1.45 % in linear trend) of the units had a significant increase in light intensity, and 1.88 % (3.33 % in linear trend) of the units had a significant decrease. Compared to period 1, the proportion of significantly changed and unchanged units decreased significantly in period 2, while non-significant units increased substantially, which could be related to the greatly improved sensitivity of the VIIRS sensors. In terms of the spatial distribution of the significantly changed units, the significantly increased units were mainly distributed in the Middle East,

Israel, Bahrain, Qatar, the UAE, Singapore, northern India, eastern China, Korea, etc., while the significantly decreased units were mainly concentrated in the east-central part of the United States, the western part of Europe, the north-western part of India, the southern part of Japan, and the Russian Far East.

Fig. 6 demonstrates the standard light trend dynamics layer SNID_{fp} for the full-period (1992–2020) based on the SNID_{p1} and SNID_{p2} after logical combinations. According to the previously developed logical combination rules, the sixteen types from the linked SNID_{p1} and SNID_{p2} were merged into five types according to the scenarios predefined in Fig. 2. From the results, about 68.03 % of the grid units globally showed a constant level of light intensity during the full-period (almost all of them were 0), and the percentage of units that did not change significantly was about 29.25 %, which closely matches the percentage of SNID_{p2}. The significantly increased units accounted for 1.76 % of the total and were mainly located in eastern Asia, north-western Europe, and especially along the eastern coast of China. The percentage of units

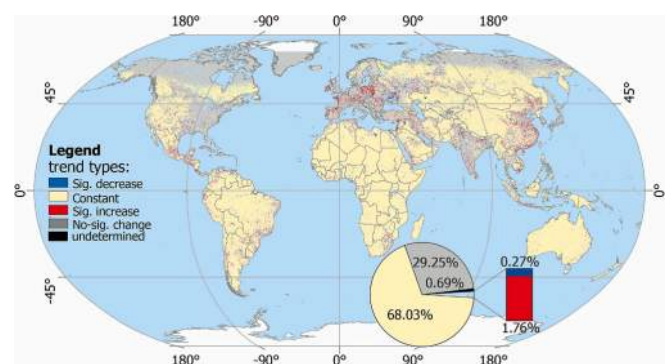


Fig. 6. The global standard light intensity trend layer (SNID_{fp}) generated based on SNID_{p1} and SNID_{p2} via logical link rules.

with a significantly decreased light intensity was 0.27 %, which was slightly lower than $ENID_{PCNL}$, mainly distributed in the Eastern European region. The rate of undetermined trends (plotted as black cells in the figure) was 0.69 %, mainly found in the Russian Far East, Northwest India, etc. These undetermined units consisted of three combinations, “significant decrease-significant increase” ($-+$, about 0.01 %), “significant increase-significant decrease” ($+-$, about 0.43 %), and “constant 0-significant decrease” ($=-$, about 0.24 %).

4.2. Full-period light intensity trend characteristics of ENTL products

Fig. 7 illustrates the distribution and percentages of the six-representative cross-sensor calibrated ENTL products after trend analysis: LiNTL, PCNL, NechaevNTL, ChenNTL, MaNTL, and PANDA. Among them, LiNTL, PCNL, NechaevNTL, and ChenNTL provide global coverage, while MaNTL and PANDA only provide data for China. It should be highlighted that ChenNTL provides temporal coverage of data from 2000 to 2020, whereas other ENTL products provide coverage from 1992 to 2020.

For LiNTL's full-period trend layer (referred to as $ENID_{LiNTL}$), about 50 % of the units were identified as constant, 20 % as non-significantly changed grid units, more than 30 % of the units were significantly increased, and about 1.5 % of the units exhibited a significant decreasing trend. Among them, the significantly decreasing units (plotted in blue) were mainly located in eastern and western Europe, the northeastern United States, central Canada, etc., while the significantly increasing units (plotted in red) were distributed globally but were mainly concentrated between $45^{\circ}N$ and $45^{\circ}S$, especially at $45^{\circ}N$, which formed a conspicuous demarcation line. For $ENID_{PCNL}$, the percentage of constant units was 91.4 %, while non-significantly changed units were only 2.19 %, and significantly decreased and increased units accounted for 0.41 % and 6 %, respectively. Compared to $ENID_{LiNTL}$, the percentage of significantly changed units decreased dramatically, especially the significantly increased units, which were only 7.2 %. In terms of spatial distribution, the significantly increased units in $ENID_{PCNL}$ were mainly found on the eastern coast of China, India, Europe, and the southeastern United States, while the significantly decreased units in blue were

mainly distributed in the northeastern United States and eastern Europe. For $ENID_{NechaevNTL}$, the percentage of constant units was 78.44 %, the percentage of non-significantly changed units was 10.85 %, and the percentage of significantly decreased and increased units were comparable at 5.04 % and 5.67 %, respectively. More specifically, the percentage of significantly increased units was similar to that of $ENID_{PCNL}$, but there was a substantial gain in the percentage of significantly decreased units, which were mainly located in the eastern United States, central Canada, northern and eastern Europe, northwestern India, and Japan and South Korea in East Asia. For $ENID_{ChenNTL}$, the percentage and distribution of each type were relatively similar to those of $ENID_{PCNL}$, with 92.33 % and 2.82 % of constant and non-significant units, respectively, and 0.26 % and 4.59 % of significantly decreased and increased units, respectively. In fact, given that $ENID_{ChenNTL}$ was calculated for the full-period (2000–2020) which differed from $ENID_{PCNL}$ (1992–2020), it was reasonable to observe a slight drop in the percentage of significant changes and a slight rise in the percentage of non-significantly changed units. In addition, ChenNTL limited its data coverage to higher latitudes, which is also a possible reason for the difference in the percentages.

At the regional scale, $ENID_{MaNTL}$ and $ENID_{PANDA}$, however, presented different results for the shares compared to the global scale. As the region with the strongest urbanization levels and economic development growth rates in the world over the past 30 years, China has experienced a significant and widespread increase in the intensity of artificial light. As a result, the percentage of units with significantly increased light intensity for $ENID_{MaNTL}$ and $ENID_{PANDA}$ in the full-period amounted to 39.66 % and 25.91 %, respectively, which is substantially higher than the global average, while the percentage of units with significantly decreased light intensity was closer to $ENID_{PCNL}$ and $ENID_{ChenNTL}$, with 0.53 % and 0.35 %, respectively. Spatially, the significantly increased units were concentrated in the east and south of China, where $ENID_{MaNTL}$ was more densely and extensively distributed, while the significantly decreased units were mainly distributed in the central part of Shanxi Province and Liaoning Province, with Linfen City of Shanxi Province being the most intensive allocation area. Linfen City is a representative resource-based city, the traditional industries (coal, coke,

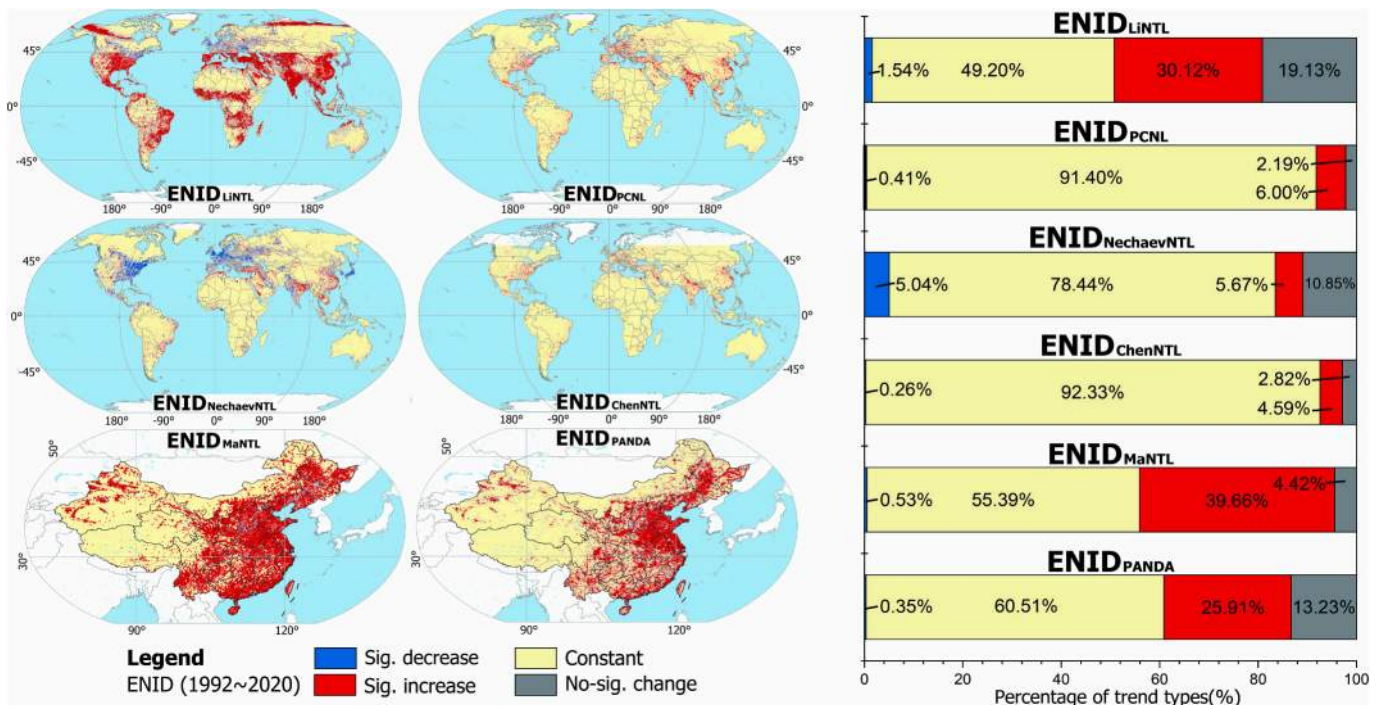


Fig. 7. The six-representative cross-sensor calibration ENTL products trend identification results ($ENID$ layers) and their percentages of each trend type.

iron, electricity, etc.) accounted for about 90 % of the industrial value-added. With the transformation of industry in recent years, its economic development is facing greater pressure.

Generally, although the above ENTL products have been cross-sensor and interannual calibrated to align the long time-series light data as well as possible, there are still noticeable differences between these products, not only globally but also in the Chinese region. Therefore, it is necessary to implement consistency analysis and assessment of the above data to better reveal the possible differences and risks of these products and thus provide a data quality reference for follow-up long-term series applications.

4.3. ENTL products consistency quality assessments based on logical diagnostic rules

Based on the full-period standard trend layer $SNID_{fp}$ shown in Fig. 6, we analyzed the six ENTL products listed above to export the corresponding light trend identification layer (LTIL) with the previously designed logical diagnostic rules (Fig. 3(b)). According to the matched results of the trend types, the consistency characteristics of grid units in ENTL products were categorized into six types, as shown in Fig. 8, including two matched types (SS matched (SS-M) and NN matched (NN-M)), three unmatched types (NS-UM, SN-UM and SS-UM), and undetermined types (UD). Among the three unmatched types, “SN-UM” and “SS-UM” deserve greater weight in LTIL as they were recognized as significant trends in $SNID_{fp}$, which made them more robust and reliable.

There are pronounced differences in the consistency characteristics among the ENTL products. For $LTIL_{LiNTL}$, the matched units accounted for a total of 52.81 %, while the unmatched “SN-UM” and “SS-UM” accounted for 11.05 % and 13.35 %, respectively, which were the highest percentage of all ENTL products. Spatially, the “SS-UM” units (plotted in red) were distributed between 45°N and 45°S, with a particular cluster in Africa and Central Asia. In $LTIL_{PCNL}$, the proportion of matched units reached 69.87 %, with “SS-M” types, which detected exactly the same type of significance trend in both the $SNID_{fp}$ and the $ENID_{PCNL}$, accounting for 68.98 %. Meanwhile, “SN-UM” and “SS-UM” account for only 0.08 % and 1.24 % of the unmatched units, respectively, considerably less than $LTIL_{LiNTL}$. For $LTIL_{NechaevNTL}$, the

percentage of matched units reached 75.06 %, with the share of the best-matched “SS-M” remaining at 68.83 %, while the share of “NN-M” increased by about 6 % compared to $LTIL_{PCNL}$. Additionally, the proportions of “SN-UM” and “SS-UM” units among the unmatched units were 1 % and 0.47 %, respectively, which were at a quite low level. For $LTIL_{ChenNTL}$, the percentage of matched units was the highest among all four globally-covered ENTL products, reaching 84.46 %, with “SS-M” in particular accounting for the majority at 82.69 %. Meanwhile, among the unmatched units, the proportion of “SN-UM” and “SS-UM” type units were 0.12 % and 0.46 %, respectively, also at the lowest level.

$LTIL_{MaNTL}$ and $LTIL_{PANDA}$, instead, indicated the results of the consistency assessment of the China-covered ENTL products. For matched units, the percentage in $LTIL_{MaNTL}$ was 69.93 %, slightly lower than $LTIL_{PANDA}$ ’s 74.99 %. However, for unmatched units, the share of “SS-UM” units in $LTIL_{MaNTL}$ reached 14.07 %, which was quite higher than that of $LTIL_{PANDA}$ at 2.66 %, and the share of “SN-UM” units showed the opposite characteristics, with a share of 0.37 % and 7.78 %, respectively. Considering that “SS-UM” has a doubly significant level of confidence compared to “SN-UM”, a higher proportion of “SS-UM” tends to imply a higher possibility of inconsistency. The spatial distribution of the “SS-UM” units showed that they were widely distributed in the urban-rural transition area, however, a more pronounced “tile” effect was present in $LTIL_{MaNTL}$.

Fig. 9 illustrates the longitude and latitude profiles of the “SS-UM” grid units after the consistency quality assessment of the ENTL products. For the longitude profiles, it can be observed that the “SS-UM” curves of different products exhibit similar general patterns, with notable peaks at specific longitudes. All globally covered products reached their highest values near 30°E, likely corresponding to regions of high nighttime light intensity such as Europe and the Middle East. In contrast, the Chinese-covered products, MaNTL and PANDA, showed their peaks around 108°E, aligning with major urbanized regions in eastern China. The quantitative differences between products are significant. LiNTL exhibited the highest volume of “SS-UM” units, with a peak near 30°E far surpassing other globally covered products like ChenNTL and NechaevNTL. This disparity suggests that LiNTL may exhibit higher sensitivity to inconsistencies in regions with intense nighttime light activity. On the other hand, MaNTL displayed a volume approximately

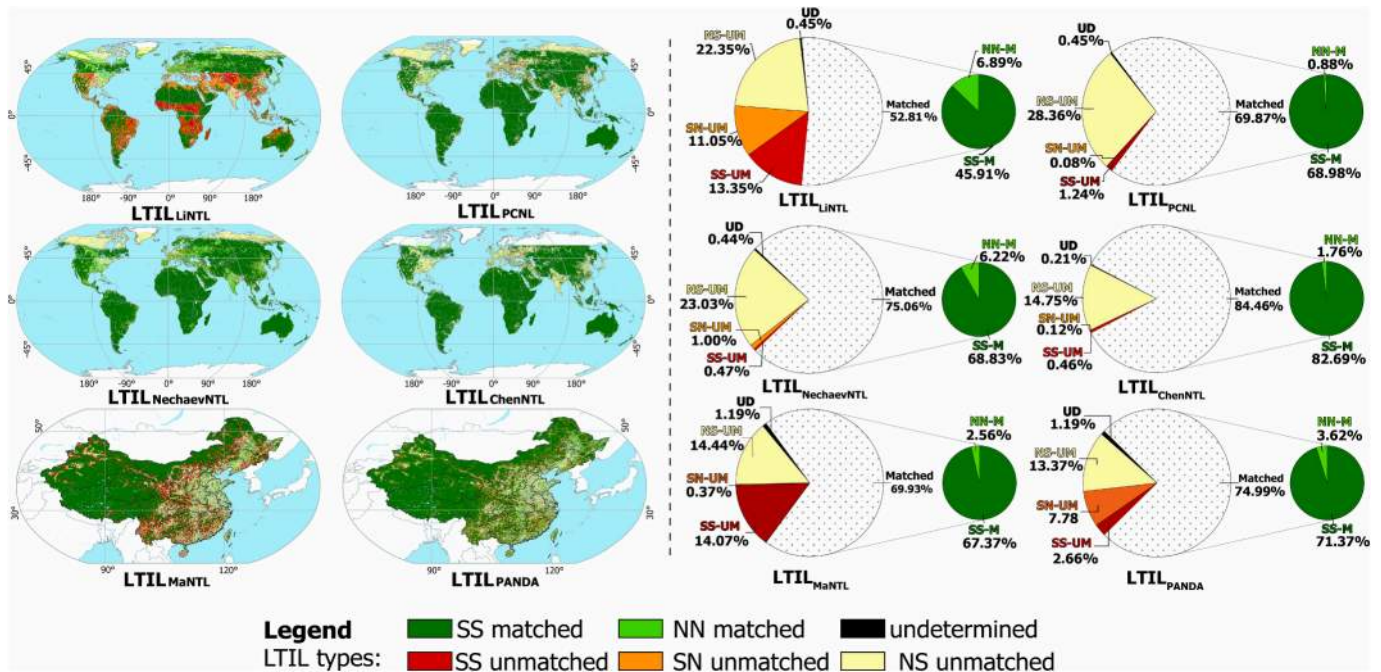


Fig. 8. The six-representative cross-sensor calibration ENTL products consistency characterization assessment results (LTIL layers) and their percentages of each consistency feature type.

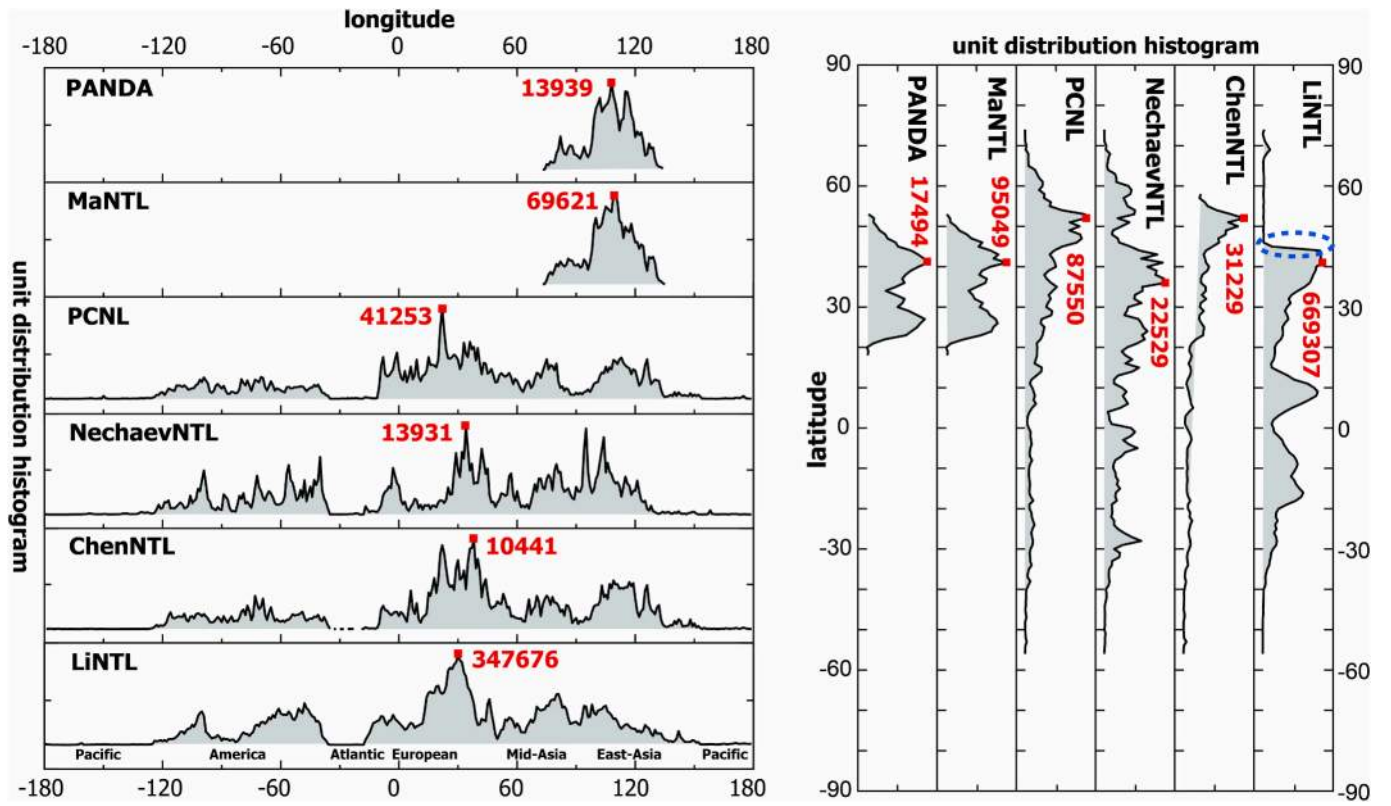


Fig. 9. Comparison of longitude and latitude profiles of consistency features of type "SS-UM" from the LTL layers (Note: the blue dotted line indicated a clear volume jump). (For interpretation of the references to colour in this figure legend, the reader is referred to the web version of this article.)

seven times greater than PANDA, reflecting its broader regional coverage and potentially higher inclusion of urban-rural transitional zones where consistency issues are more pronounced.

For the latitude profiles, the Chinese-covered products showed

similar peak locations around 40°N, corresponding to the heavily urbanized areas of northern China. Meanwhile, globally covered products demonstrated varying peak latitudes. PCNL and ChenNTL peaked above 50°N, capturing areas in northern Europe and North America, while

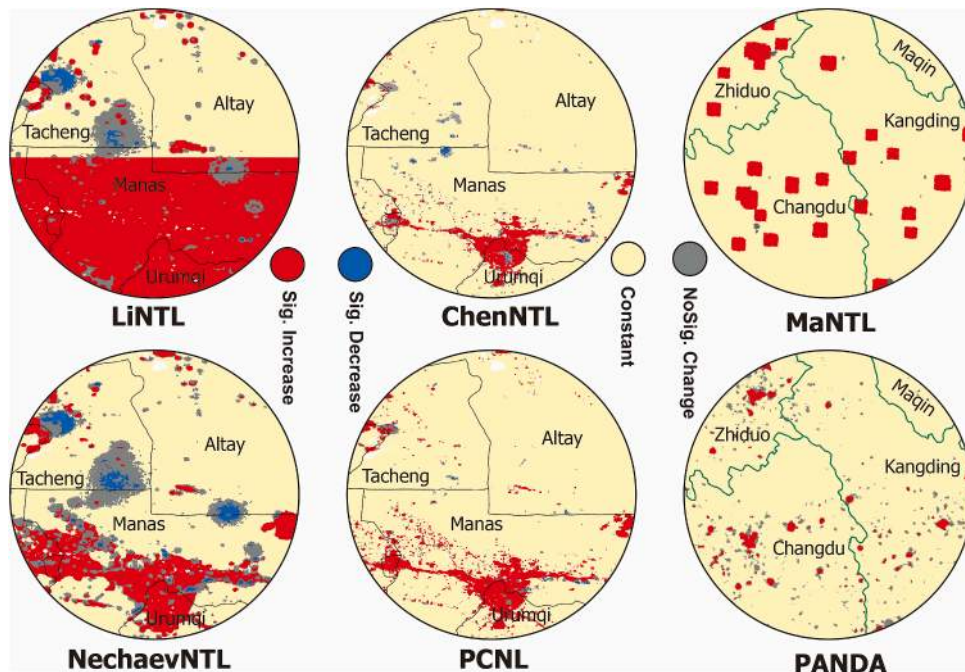


Fig. 10. Comparison of time-series dynamic types of different ENTL products in the local area (Note: A distinct variation in dynamic consistency is evident among the ENTL products: LiNTL exhibits a clear division; MaNTL shows a noticeable block effect; and NechaevNTL identifies significantly more variation units compared to ChenNTL and PCNL).

LiNTL reached its maximum at 45°N, likely reflecting urban clusters in the United States, Europe, and East Asia. NechaevNTL, however, displayed its highest values south of 40°N, suggesting differences in how it handles light intensity trends in lower-latitude regions. These patterns indicate that while the overall distribution of “SS-UM” grid units aligns with expected high-light regions, the specific product characteristics and calibration methods result in notable differences in the volume and spatial patterns of inconsistencies. Such variations underscore the importance of selecting products based on their specific strengths and limitations (as shown in Fig. 10, which illustrates the variation in time-series consistency among different ENTLs in a localized area), particularly for studies focused on regions with high spatial heterogeneity or contrasting light intensity levels.

4.4. Validation of the proposed scheme

Currently, accessible and robust third-party data to validate the reliability of the scheme proposed in this paper is still scarce. This limitation reflects the broader challenge in the NTL research field. To address this issue, we employed two successive strategies without relying on external data criteria to investigate the validity and reliability of the proposed methodology. These strategies aim to evaluate the robustness of the scheme in ensuring consistency and accuracy in ENTL product assessments.

First, to evaluate the validity and reliability of the proposed methodology, we designed a validation strategy focusing on two quality types derived from the LTIL layer: SS-Matched (SS-M) and SS-Unmatched (SS-UM). These types represent grid units with the highest and lowest consistency, respectively, in their identified light intensity trends. Based on these two consistency LTIL layer types, a random sample of 4000 units of each type was conducted globally and nationally to ensure the reliability and representativeness of the results. For each sampled units, the goodness-of-fit (R^2) values were calculated for the p1 and fp periods, and the difference ($\Delta R^2 = R^2(fp) - R^2(p1)$) was used as an indicator of trend consistency. A ΔR^2 value close to zero was interpreted as indicating that the trend identified for a grid cell in the p1 period remained highly consistent when extended to the fp period, whereas a larger positive ΔR^2 was considered to indicate trend divergence over time, reflecting potential instability. This strategy was based on the assumption that SS-M cells, due to their inherent stability, would exhibit ΔR^2 values close to zero or even negative, whereas SS-UM cells, reflecting less consistent trends, would show significantly larger ΔR^2 values. Metrics were compared across multiple ENTL products to evaluate the reliability of the proposed scheme under varying conditions.

The results, as shown in Fig. 11, demonstrate the effectiveness of the proposed scheme. For SS-M units, ΔR^2 values across all ENTL products were found to be close to zero or negative (e.g., -0.07 for LiNTL and $-$

0.11 for MaNTL), indicating that trends identified during the p1 period were reliably maintained in the fp period. Conversely, for SS-UM units, ΔR^2 values were significantly higher, with LiNTL and NechaevNTL reaching 0.67 and 0.70 , respectively. This result suggests that trends for SS-UM units identified in p1 often diverged when extended to fp, highlighting their inherent instability. The consistently low ΔR^2 values for SS-M units across all ENTL products demonstrate the robustness of the proposed scheme in preserving stable trends, while the variability in ΔR^2 among SS-UM units reflects the scheme's capability to differentiate between stable and unstable trends. Additionally, the consistent results across global and national scales validate the scalability of the scheme and reinforce its applicability for diverse contexts. These findings collectively confirm that the proposed methodology is effective in ensuring trend consistency over extended periods while providing meaningful insights into discrepancies in less consistent units.

Besides, according to the specific steps depicted in Fig. 4, we implemented self-validation based on each of the six related ENTL products, and the results are shown in Fig. 12. It can be found that ChenNTL has 96.30% of matched units, followed by PCNL and NechaevNTL with 95.41% and 90.03% , respectively, and followed by PANDA (75.66%), LiNTL (75.34%), and MaNTL (69.74%) successively. Compared to the percentage of matched units, the percentage of unmatched units is a more powerful indicator to demonstrate the effectiveness of our proposed strategy. Among them, all six ENTL products had a percentage of unmatched units less than or equal to 1.5% , especially ChenNTL, and PCNL, which had a percentage of unmatched units less than 0.1% , basically negligible. Moreover, if only “SS-UM” was counted among the unmatched units as the unmatched type with the highest level of confidence, its share of ENTL products would be further reduced to less than 0.002% , and even less than 0.0005% for MaNTL, PANDA, and PCNL. Therefore, the statistical results suggest that the proposed scheme has good reliability, especially its high accuracy for detecting “SS-M” perfectly matched and “SS-UM” unmatched units, thus it can be regarded as the key metrics in the consistency quality assessment of ENTL products.

5. Discussions

5.1. Robustness and applicability of the proposed scheme

The quality of the $SNID_{fp}$ is key to ensuring the robustness of the ENTL products consistency quality assessment results, as it was considered as a reference, or standard, for global trends in light intensity over the full-period. In this paper, we take a series of necessary steps to improve the reliability of $SNID_{fp}$. For example, four widely recognized and applied DMSP/OLS interannual NTL products were selected to derive the light intensity trends for p1, and then we kept the trend-type identical grid units for $SNID_{p1}$ using the intersection operation on the results of the four trends. The above process can effectively mitigate the grid units of pseudo-change trends and ensure the robustness of the trend types identified in the $SNID_{p1}$. In addition, in p2, we selected VNP46A2 to compute $SNID_{p2}$ as it is the current state-of-the-art NTL post-processing product after a strict and standardized calibration process by NASA Black Marble Generation protocols. Lastly, we also employed a most conservative strategy in designing the logical combination rules to derive the $SNID_{fp}$, defining any combinations that could have been misclassified as undetermined trend types (label as * in Fig. 3 (a)). Thus, for $SNID_{fp}$, it can be argued that while it does not provide a complete valid trend for all grid units, of those units already presented, any trend it indicates is highly reliable.

Also, in this paper, we have used the linear trend joint t -test and the M-K trend test to perform trend analysis on a 30 arc-seconds grid unit and to implement a consistency assessment of ENTL products through a series of designed logical combinations and diagnostic rules. A 30 arc-seconds grid unit size was adopted mainly because most of the selected ENTL products were developed and produced on this scale (e.g.,

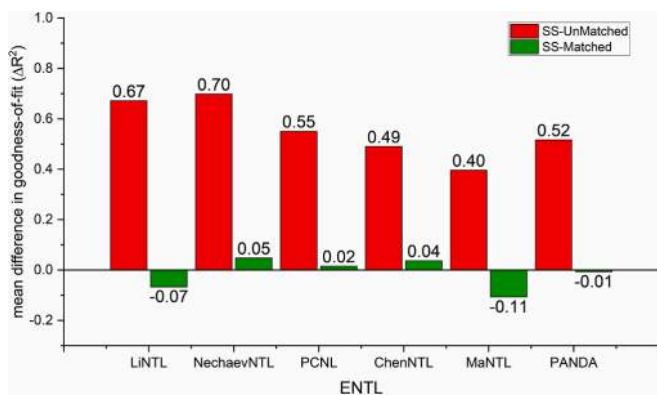


Fig. 11. Mean difference in Goodness-of-Fit (ΔR^2) for SS-M and SS-UM units across six ENTL products (Note: ΔR^2 was computed as the difference between the goodness of fit of the NTL intensities from the p1 period and the fp period).

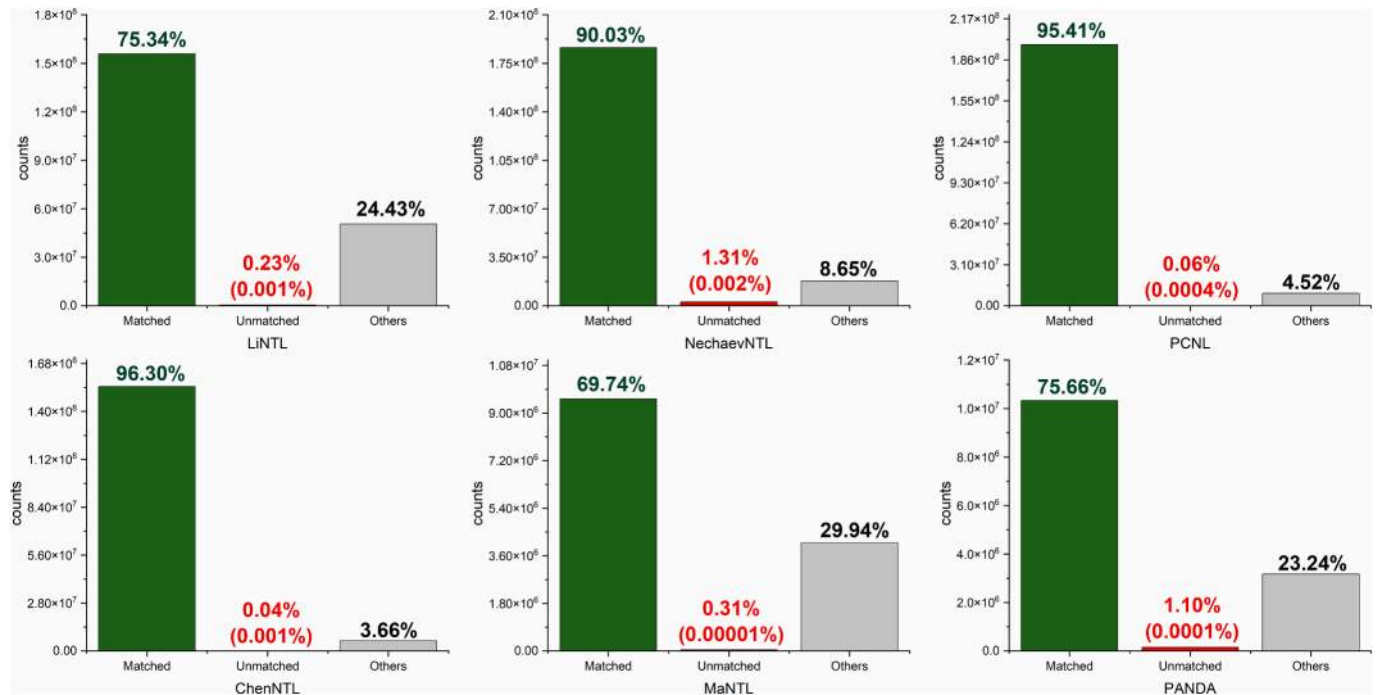


Fig. 12. The percentage of matched and unmatched types after self-validation for all six relevant ENTL products.

around 1 km at the equator), with only ChenNTL kept at 500 m resolution. Furthermore, we conducted the same analysis at the 5 arc-minutes grid unit scale to explore the impact of scale effects on trend detection results. The larger 5 arc-minutes grid unit scale analysis helps reveal more macro-level trend characteristics, aiding in examining whether similar trend distributions are maintained at larger scales, thereby enhancing the robustness of the proposed method.

The percentage of trend units of each type of SNID in different configurations is shown in Table 3. It can be found that 1) the percentages of significantly changed grid units under the M-K trend test were all lower than the linear trend analysis, and the percentages of significantly changed units under the 5 arc-minutes were all much higher than the 30 arc-seconds units; 2) for constant units, the identification of results from M-K and linear trends were broadly comparable, whereas the percentages of units at the 30 arc-seconds were higher than at the 5 arc-minutes; 3) the fraction of non-significantly changed and undetermined units were not sensitive to trend detection methods but increased with unit scales.

Further, based on the different configurations listed above, the consistency of ENTL products was evaluated using logical diagnostic rules, and the results were tabulated as follows. It can be seen that there are certain differences in the proportion of consistency types recognized at different scales. It is worth noting that the “SS-M” and “SS-UM”, which characterized the best and least consistency levels, presented a consistent pattern, i.e., all ENTL products at a 30 arc-seconds unit scale revealed a larger share. In contrast, “SS-UM” showed differences, for

example, LiNTL, PCNL, NechaevNTL, and MaNTL had a larger share for 30 arc-seconds units, while ChenNTL and PANDA achieved a larger share for 5 arc-minutes units. In addition, we attempted to construct an index q to more intuitively invert the consistency level of the ENTL products by applying the ratio of matched to unmatched units ($q = \frac{SS_M + NN_M}{SS_UM + SN_UM}$). The results suggested that ChenNTL achieved the greatest advantage under either unit scale, while LiNTL was inferior in comparison.

Conclusively, although different unit scales cause variations in the proportion of consistency types, for the most critical consistency indicators, “SS-M” and “SS-UM”, larger unit scales tend to increase the risk of overestimation of “SS-M”, and in specific scenarios lead to an underestimation of “SS-UM”. In addition, considering that the 30 arc-seconds unit is more closely aligned with the spatial resolution of the ENTL products itself, it can more accurately and finely reveal the spatial distribution differences in consistency compared to the 5 arc-minutes unit, as shown in Fig. 13.

Also, it should be noted that ChenNTL only provided time-series images after 2000, so we updated the time-series images used in the calculation of SNID_{p1} (i.e., images for the period 2000–2012 were used instead of 1992–2012), thus minimizing the risk of misidentification when matching the ENID_{ChenNTL}. Updates on SNID are necessary because the results of consistency quality assessments can be clearly biased by differences in SNID. This bias is illustrated in Fig. 14, where the blue bars show the results of the consistency quality assessment based on the updated SNID, while the red bars show the assessment

Table 3

Percentage of each type in the identified SNID under the linear and M-K trend analysis for 30 arc-seconds and 5 arc-minutes units.

Configure	Sig. increase			Sig. decrease			Constant			Non-sig. Change			undetermine
	p1	p2	fp	p1	p2	fp	p1	p2	fp	p1	p2	fp	
Period ^a													
Linear 30 ^b	5.38	1.45	2.04	0.50	3.33	0.28	87.11	68.42	67.82	7.01	26.80	28.62	1.24
M-K 30 ^c	5.01	1.23	1.76	0.49	1.88	0.27	87.38	68.42	68.03	7.12	28.47	29.25	0.69
Linear 5'	11.71	3.63	2.85	1.26	7.90	0.44	74.29	42.90	42.27	12.74	45.57	50.61	3.83
M-K 5'	11.57	3.22	2.57	1.25	8.18	0.44	74.46	42.90	42.36	12.72	45.70	50.42	4.20

^a p1 refers to period 1 (1992–2012), p2 refers to period 2 (2012–2020), and fp refers to full-period (1992–2020).

^b 30" refers to 30 arc-seconds, and 5' refers to 5 arc-minutes.

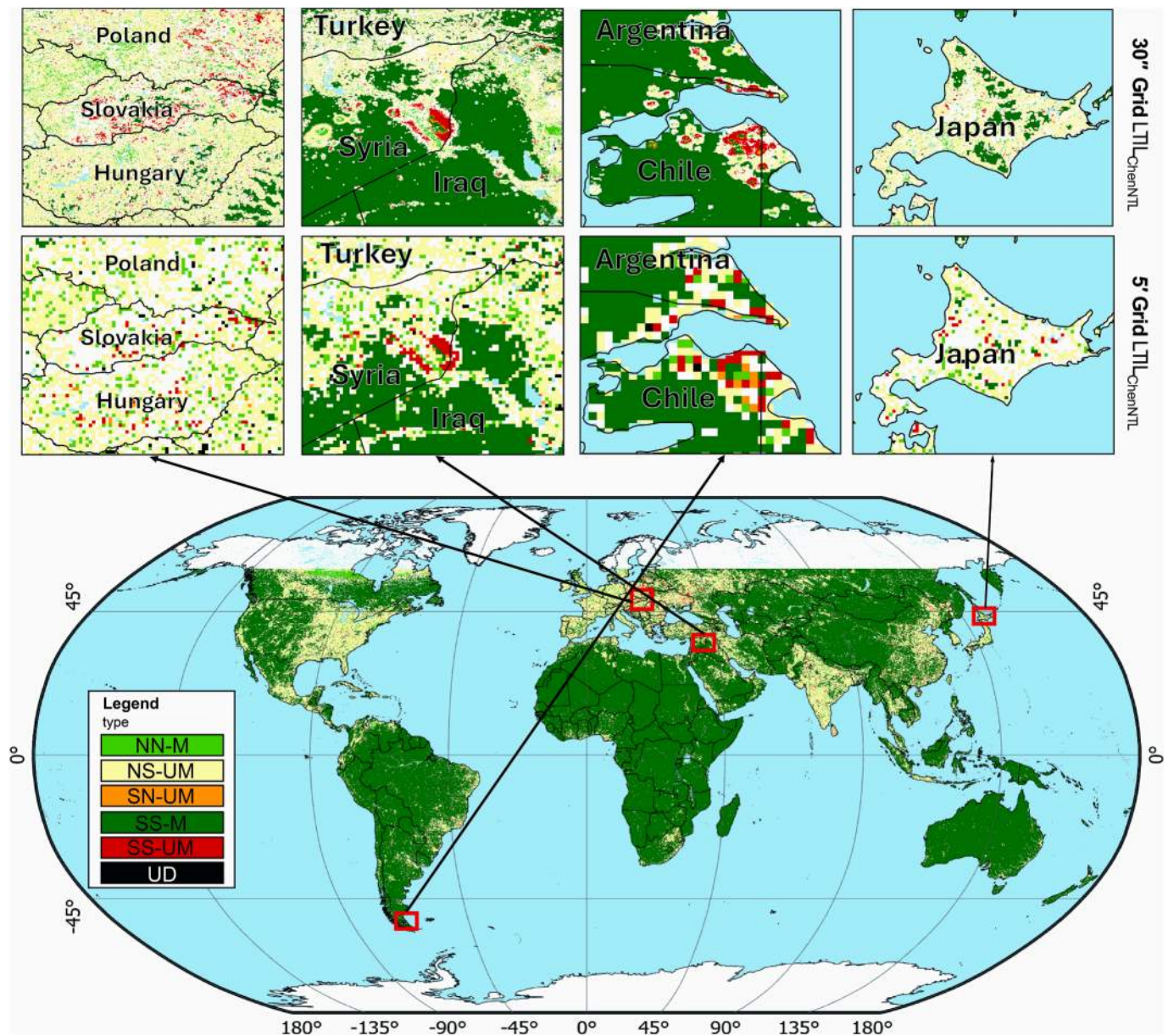


Fig. 13. Comparison of LTL identification results for ChenNTL at 5-arcminute and 30-arcsecond unit scales.

based on the non-updated SNID. It can be observed that the non-updated scheme leads to an underestimation of the amount of matched units and a substantial overestimation of unmatched units compared to the updated strategy.

5.2. ENTL product consistency variations and potential sources

To better understand the similarities and differences among the ENTL products, we calculated a consistency percentage matrix based on the overlap of “SS-Matched” and “NN-Matched” units (Fig. 15). This matrix provides a quantitative measure of how well the datasets align in capturing nighttime light trends. By examining these relationships, we can highlight patterns of agreement and divergence among the products, offering valuable insights for researchers when selecting datasets.

Overall, globally covered products, such as ChenNTL, NechaevNTL, and PCNL, exhibit high pairwise consistency percentages, typically exceeding 90 % (e.g., ChenNTL vs. NechaevNTL: 91.90 %, NechaevNTL vs. PCNL: 89.83 %). This strong alignment suggests that these datasets are robust in their calibration and are well-suited for global analyses. In

contrast, LiNTL shows lower consistency with other datasets (e.g., LiNTL vs. ChenNTL: 57.72 %), reflecting its distinct calibration strategies and sensitivity to light intensity variations, particularly in regions with greater spatial heterogeneity. For region-specific products, particularly those focusing on China (e.g., PANDA and MaNTL), the consistency percentage between them is relatively high (77.99 %), indicating strong alignment in capturing local trends. However, their consistency with global datasets is somewhat lower (e.g., PANDA vs. ChenNTL: 81.37 %; MaNTL vs. ChenNTL: 77.52 %), likely due to differences in how regional and global datasets handle localized variations in light intensity.

Building on the global consistency analysis, it is also important to consider how these differences manifest at more specific regional and national scales. While the overall consistency percentage matrix provides a broad understanding of inter-product similarities, regional variations often reveal product-specific calibration strategies and their adaptability to localized conditions. For example, differences in matched unit ratios across specific regions and countries can further illustrate the strengths and limitations of each dataset when applied to finer spatial scales, as detailed in Fig. 16. All six products exhibit strong

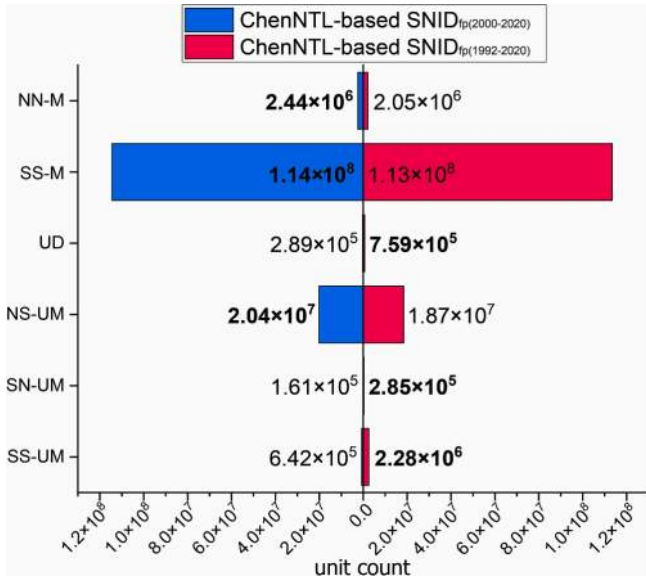


Fig. 14. Comparison of the number of consistency feature types in LTIL before and after the $SNID_{ip}$ updated.

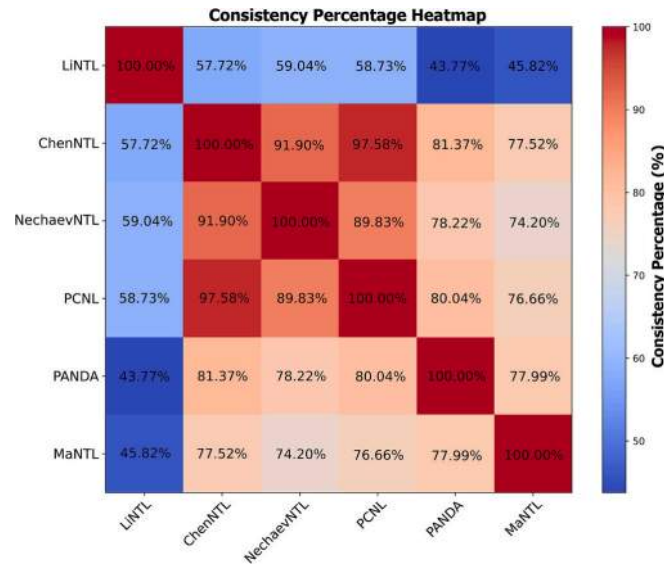


Fig. 15. Consistency percentage matrix of ENTL products (Note: The values represent the proportion of “SS-M” and “NN-M” units shared between the pairs of datasets; higher percentages suggest stronger alignment in nighttime light trends, whereas lower percentages reflect divergence in calibration methods or sensitivity to specific regions).

consistency in low-light regions with stable light signals and minimal dynamic sources, such as African countries (e.g., Niger, Mauritania) and western provinces in China (e.g., Tibet, Qinghai), where matched ratios exceed 0.8. In medium-brightness regions, such as South America (e.g., Bolivia, Peru) and central China (e.g., Hunan, Guizhou), ratios range from 0.5 to 0.9, with ChenNTL and PCNL performing slightly better due to their advanced calibration methods. By contrast, in highly urbanized and high-light pollution regions, such as the United States, parts of Europe, and China’s eastern coastal provinces (e.g., Shanghai, Jiangsu), matched ratios decline significantly (<0.5), reflecting challenges posed by dynamic light sources and complex urban lighting. PANDA and ChenNTL, however, show relatively better performance in such regions, likely due to their enhanced sensitivity to dynamic signals.

These observations highlight the need for algorithmic improvements

to better address the challenges of dynamic light sources and high-light pollution areas. Regionalized calibration strategies tailored to varying light characteristics, such as adaptive filtering thresholds for weak-light regions or dynamic source corrections for urban cores, could enhance product reliability. Additionally, integrating multi-source data, including ground-based measurements and high-resolution imagery, could complement existing datasets and improve consistency evaluations. While all products perform well in stable, low-light regions, PANDA and ChenNTL have demonstrated superior adaptability in high-pollution and complex environments, making them preferable choices for such areas. Continued optimization is essential to expand the applicability and reliability of ENTL products across diverse geographic settings.

Overall, the consistency variations observed across different ENTL products, both within the same region and across different regions, underscore the complex interplay of factors influencing calibration performance. These variations can primarily be attributed to two aspects: (1) the inherent diversity of surface NTL radiation, especially in high-intensity NTL regions where dynamic light sources, saturation effects, and reflective interference present significant challenges to calibration models. Such challenges yield varying impacts depending on the calibration strategies employed; (2) the discrepancies in data processing workflows among different ENTL calibration models, such as the thresholds for masking background noise, the selection of correction functions, and the choice of pseudo-invariant target areas. These methodological differences inevitably lead to performance gaps between products in regions with distinct lighting characteristics (Table 4, Table 5).

Specifically, products such as ChenNTL and PANDA typically exhibit relatively better performance among ENTL products globally and regionally, respectively. Chen et al. (2020) utilized an auto-encoder model enhanced with NDVI data to reduce background noise and improve consistency in low-brightness regions. Similarly, Zhang et al. (2024) employed a convolutional LSTM network combined with temporal smoothing (RLOWESS) to capture spatiotemporal dynamics and enhance long-term consistency. These approaches excel in handling complex scenarios, such as regions with significant brightness variability or temporal fluctuations. In contrast, regression-based methods, while straightforward and effective for certain regional or simpler calibration scenarios, may encounter challenges in addressing non-linear dynamic ranges and overglow effects in more complex environments, such as urban cores or rapidly developing regions. These methods might require further refinement to fully adapt to diverse geographic conditions. Geographic factors also contribute to differences in product performance. For instance, urban areas can exhibit overglow effects, and rural regions may be more influenced by background noise, highlighting the importance of robust noise reduction strategies. Additionally, high-latitude regions, influenced by unique natural phenomena such as polar nights and solar contamination, can pose specific calibration difficulties that benefit from tailored approaches.

Furthermore, these challenges point to broader issues in ENTL calibration and consistency evaluation. The diversity of NTL radiation patterns suggests the need for regionalized calibration approaches tailored to the characteristics of specific environments. For instance, adaptive thresholds could be applied to weak-light regions to enhance noise filtering, while more robust correction algorithms might be required to handle dynamic light sources in urban cores. Multi-source data fusion, integrating ISS (International Space Station) nighttime imagery, high-resolution satellite observations, or ground-based measurements, could further complement existing datasets to address discrepancies in complex environments.

5.3. Potential analysis of the proposed scheme

In the scheme presented in this paper, logical combinations and diagnostics were performed based on the type of trend of the unit during



Table 4

Product	Source of background noise	Noise processing method	Strengths	Limitations
LiNTL	Dynamic range differences and background noise	Statistical regression (S-shaped function) and regional calibration	Simple and globally applicable	Limited capacity for localized noise handling
PCNL	Urban boundary fuzziness, extreme high and low values	Outlier removal, masking low-value areas, regression-based adjustment	Focuses on pixel-level consistency; suitable for fine-scale studies	May leave residual extreme outliers
NechaevNTL	Resolution differences, sensor noise	Residual learning with U-Net convolutional neural network	High automation and effective noise reduction	Sensitive to training data quality
ChenNTL	Low-brightness errors, sensor inconsistencies	Image enhancement with NDVI and feature extraction through Auto-Encoder	Significant improvement in spatial quality; strong feature extraction	Relies heavily on high-quality auxiliary data like NDVI
MaNTL	DMSP overglow effect, satellite drift	Dynamic range adjustment and noise smoothing via BiDoseResp model	Effectively addresses overglow; strong dynamic range adaptation	Complex parameter tuning, limited global applicability
PANDA	Temporal fluctuations in long-term sequences	Temporal smoothing using convolutional LSTM and RLOWESS	Strong temporal consistency; robust modeling of long-term changes	High computational complexity

the long-term time series so as to identify the consistency features and their spatial heterogeneity among the ENTL products. We reduced the computational effort and increased the applicability of the model by “summarizing” the diverse characteristics of light intensity changes into a limited number of four types, including significantly increased, significantly decreased, constant, and non-significant changes. This process implements an information compression of the light change characteristics that allow for rapid execution of logical operations, which ultimately results in a global 30'' unit scale consistency quality assessment. For assessment results, the “SS-M” type means the highest level of consistency quality as there are consistent trends of significance detected in both SNID and ENTL products. In other words, the proposed scheme can effectively answer the concern of what is matched and what is not matched in ENTL products, but can it further indicate what is well-matched and what is moderately matched?

For this question, we conducted a further categorization of the matched grid units based on the proposed scheme and tried to answer

this concern. Specifically, for the matched units in ENTL products, the trend-analyzed slopes (Sen's slope in M-K) were extracted for each of their p1 and p2 periods, and then their matching degree was indicated further by evaluating the absolute difference of the slopes over the two sessions. In Fig. 17, the slope differences of the matched units are categorized into five levels (Perfect, Good, Fair, Poor and Low Match) automatically based on the Natural Break method, and the average slopes for different match levels of units were counted separately for the p1 and p2 periods (additionally, the annualized slope profiles were plotted for the "Low" match units which had the the largest differences). It can be found that 1) the slopes during the p2 period were substantially higher than those during the p1 period for almost all matching levels of the ENTL products; 2) the slope gap between the p2 and p1 periods decreased as the matching quality improved; 3) the slope of the p2 period of ChenNTL was significantly higher than that of the other ENTL products, but it rapidly declined and gradually approached the p1 period slope as the matching quality improved. We speculate that since

Table 5

Comparison of cross-sensor calibration models/strategies for six ENTIL products.

Product	Calibration model/Strategy	Description	Strengths	Limitations
LiNTL	S-shaped function	Uses nonlinear fitting with sigmoid functions to convert VIIRS data into DMSP-like data for consistent time series	Simple and suitable for global-scale applications	Limited handling of local complexities
PCNL	Regression models (various forms)	Pixel-level calibration using statistical regression (e.g., polynomial, linear regression) while maintaining temporal and spatial consistency	Simple and effective; suitable for pixel-level studies	Insufficient for complex nonlinear relationships
NechaevNTL	Residual U-Net neural network	Learns the mapping between DMSP and VIIRS through convolutional neural networks to generate DMSP-like images	Strong capability for nonlinear modeling; adaptable to complex scenarios	Computationally intensive; high dependence on training data
ChenNTL	Auto-Encoder	Extracts shared features of DMSP and NPP data through Auto-Encoder for cross-sensor calibration	Highly automated; strong feature extraction capabilities	Requires high-quality auxiliary data such as NDVI
MaNTL	BiDoseResp model (weighted sigmoid function)	Combines flexibility of sigmoid functions, fitting separately for low and high brightness regions	Strong dynamic range adaptation; effective for bright and dim areas	Complex parameter tuning; limited regional scalability
PANDA	Convolutional LSTM combined with RLOWESS	Captures spatiotemporal dynamics with convolutional LSTM and smoothens temporal sequences using RLOWESS	Strong spatiotemporal modeling; excellent temporal consistency	High computational requirements

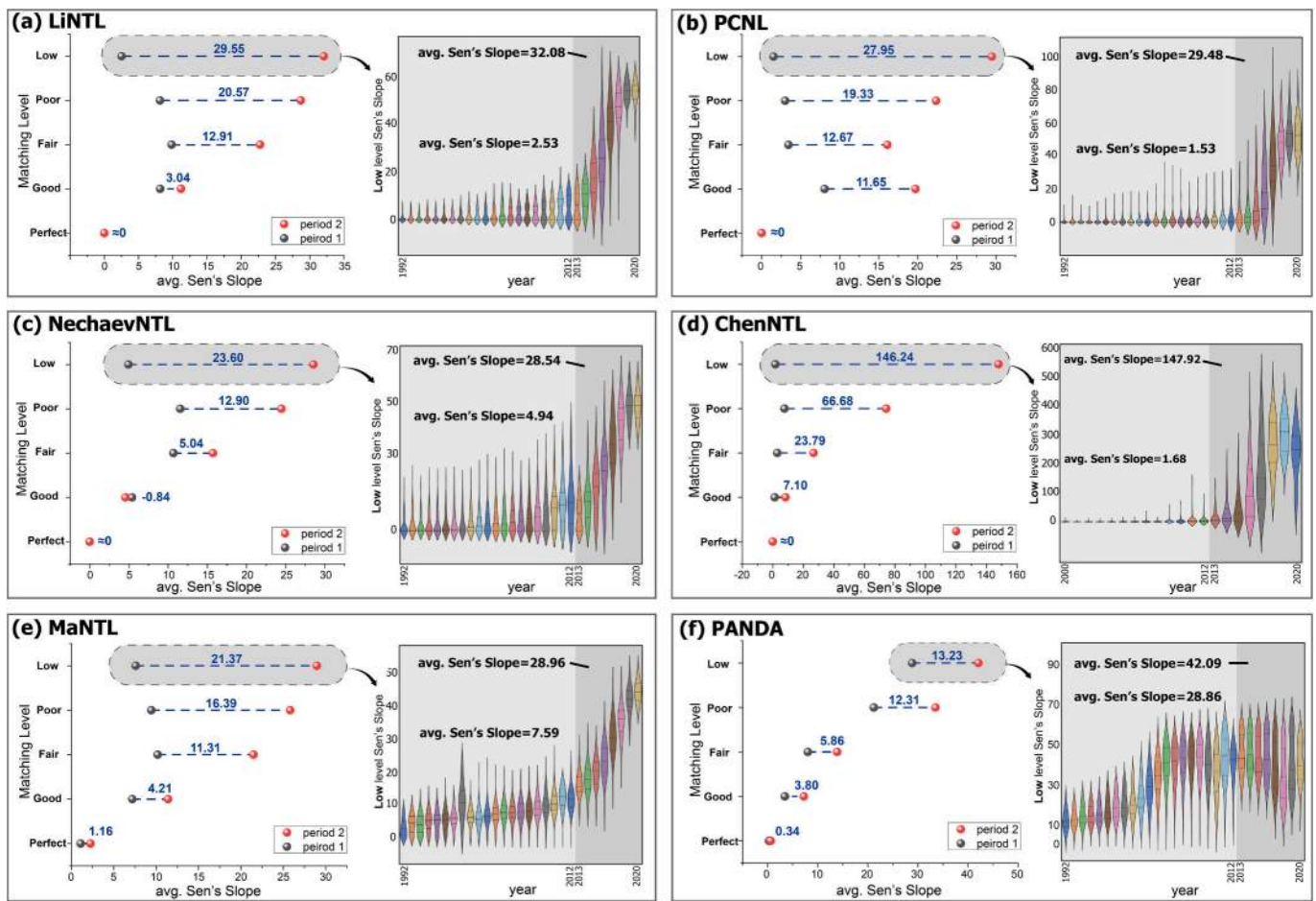


Fig. 17. Means and gaps of Sen's slope for each match level between period 1 and period 2 (Note: the blue numbers labeled the mean Sen's slope difference between the 2 periods; the violin plots in the right panel of each ENTIL product showed the annual slope characteristics of the "Low" matching level units). (For interpretation of the references to colour in this figure legend, the reader is referred to the web version of this article.)

ChenNTL employed the exact opposite ENTIL products synthesis strategy, i.e., using the NPP/VIIRS product as a baseline to generate VIIRS-like data. The benefits of this scheme are obvious, preserving the advantages of the VIIRS sensor, such as higher spatial resolution, good radiosensitivity, non-saturation, etc., however, it also leads to the fact that ChenNTL tends to have higher values and increases in the p2 period compared to other ENTIL products. Nevertheless, the proposed scheme in this paper is effective in identifying the consistency features of finer-

scale light intensities, and, together with the slope level, the scheme has the potential to assess the matching quality.

Besides, with the continuous development and updating of ENTIL products in the future, the $SNID_{fp}$ constructed for the period 1992–2020, as described above, will no longer be fully applicable to the latest datasets. However, due to the good adaptability and extensibility of the proposed scheme, it can be updated dynamically by recalculating $SNID_{p2}$ using the most recent ENTIL products. To demonstrate this

capability, the SNID_{fp} was updated to include NTL data up to 2024, leveraging the near-real-time updates of the VNP46A2 product. This extension expands the monitoring period from 1992 to 2020 to 1992–2024 without requiring modifications to the original framework, showcasing the scheme's potential for real-time or near-real-time consistency assessments. The results are shown in Fig. 18, where (a) shows the distribution of SNID_{fp} for the period 1992–2020, (b) shows the updated SNID_{fp} for the period 1992–2024, and (c) highlighting the type-transition relationship between the two periods. It can be observed that even though the type proportions of SNID_{fp} have been updated slightly with the inclusion of new data, the overall stability remains high, with the vast majority of units maintaining their original identified type in short-term updates. This analysis highlights the potential of the proposed scheme not only for historical evaluations but also for dynamic monitoring applications. Its flexibility in integrating newly available datasets ensures its applicability to evolving NTL products, thus enhancing its relevance for long-term and real-time consistency assessments.

5.4. Implication and limitations

The ENTL products, through the development of specific technical tools such as algorithmic calibration, mathematical modeling, and artificial intelligence techniques, combine NTL data from different satellite sensors to create a continuous and temporally consistent NTL dataset. The availability of NTL data records over a much-extended time span helps researchers more accurately analyze and understand changes in NTL intensity, making it possible to apply the data to a wide range of research and practice scenarios, such as urban extension studies, disaster monitoring, and environmental change assessment. While, the time-series consistency of NTL intensity, as the most central quality parameter of ENTL products, directly affects the accuracy and reliability of studies and applications based on these data. For example, for long-term urban development studies, environmental monitoring or economic growth analyses, consistent time-series data can provide more accurate

trend analyses and pattern predictions. Therefore, the consistency quality assessment scheme developed in this study and the SNID layer generated thereby can be regarded as an essential data quality reference for subsequent practical applications of ENTL products. This scheme, based on dynamic trends and logical rules, provides a precise and efficient consistency inspection approach for ENTL products, which greatly improves the reliability and practicability of the data in various applications as compared to the previous subjective selection of TSOL metrics for regional statistics. Broadly stated, our approach optimizes the consistency quality assessment process of ENTL data, not only extending its validation samples' coverage on a global scale, but also greatly improving the fineness of the inspection and achieving grid-scale validation, which is particularly crucial for global NTL emission change monitoring and pattern recognition that requires long-term series data support. Particularly for ENTL-based urban mapping, accurate time-series consistency of NTL intensities allows for a more accurate depiction of the expanding and shrinking of urban boundaries, identification of the internal structure of cities, assessment of the environmental impacts of the urbanization process, and effective urban planning policies to understand and cope with the challenges posed by urbanization. Fig. 19 illustrates a typical case scenario in which the consistency of NTL intensity in ENTL products has deteriorated as the statistical scale of the study area has been reduced. Specifically, we selected three case areas at different scales in northern, central, and southern China and then exported the NTL consistency profile curves based on LiNTL and ChenNTL from the provincial, city, and county levels, respectively. According to the coefficients and R^2 of the linear fit function for each curve segmentation can be clearly found: 1) almost all of the curves experienced an abrupt change in slope (even reversed in direction) as the curves moved from the p1 portion into the p2 portion; 2) and the magnitude of the shifts becomes more pronounced as the scale of the statistical units shrinks from the provincial to the county level. This result demonstrates that there is a scale effect on the consistency quality of ENTL products, and that at finer scales, this concern deserves more attention.

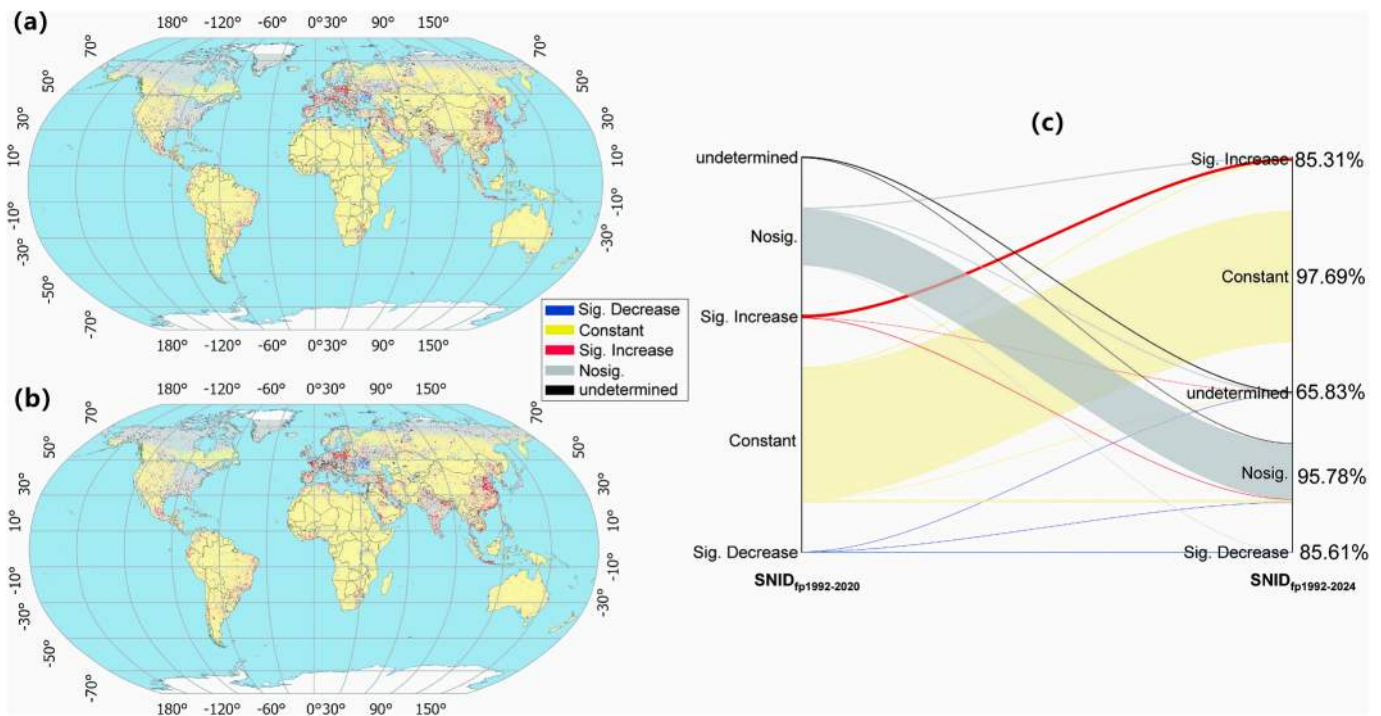


Fig. 18. Distribution and type transition of SNID_{fp} generated based on 1992–2020 and 1992–2024 NTL products, respectively (Note: (a) SNID_{fp}1992–2020, SNID_{fp} distribution for 1992–2020; (b) SNID_{fp}1992–2024, SNID_{fp} distribution for 1992–2024; (c) type transition relationships between SNID_{fp}1992–2020 and SNID_{fp}1992–2024, with the proportion of stable type transitions (type unchanged) shown on the right y-axis).

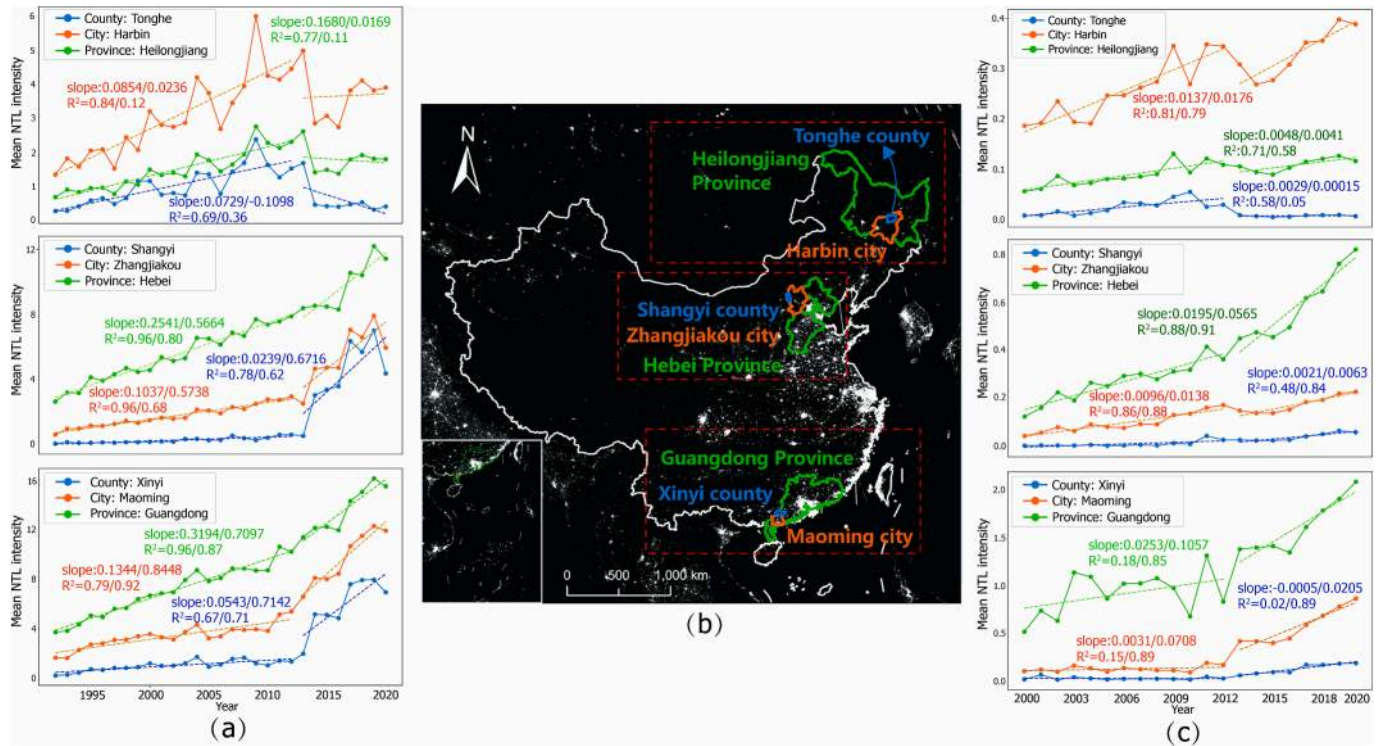


Fig. 19. Time-series dynamic profiles of NTL intensity in three case regions of China (Note: (a) NTL intensity dynamics profiles from LiNTL products for 1992–2020 at three different scales: provincial, city, and district; (b) the location map of the three case regions in China; (c) NTL intensity dynamics profiles from ChenNTL products for 2000–2020 at three different scales: provincial, city, and district; for each scale of the consistency curves, a segmented linear fit was applied and the slopes and R^2 of the functions for the p1 and p2 periods were labeled).

Meanwhile, for dimly lighted regions such as suburbs, the consistency concerns for ENTIL products would seem to be more obvious compared to urban areas where NTL densities were more concentrated. To visually depict this difference, we extracted separate urban and rural masks from the latest NPP/VIIRS imagery based on a simple fixed thresholding method and applied them to the LTIL layers, and the results are shown in Fig. 20. It was found very intuitively that the percentage of unmatched units that were identified in all LTIL layers showed drastic differences between urban and rural areas, where the unmatched units

in urban areas was almost negligible. Also, in terms of urban areas, the matched units contribute the vast majority, especially for LiNTL and ChenNTL, which account for more than 99.5 %. This considerable consistency gap between urban and rural areas may be closely related to the specifications of the upstream products of ENTIL, i.e., DMSP/OLS and NPP/VIIRS. For instance, the low sensitivity and spatial resolution of DMSP/OLS limit its applicability in rural or low-light-density regions. In contrast, newer sensors like NPP/VIIRS have higher sensitivity and resolution, enabling them to capture changes in weak light sources and

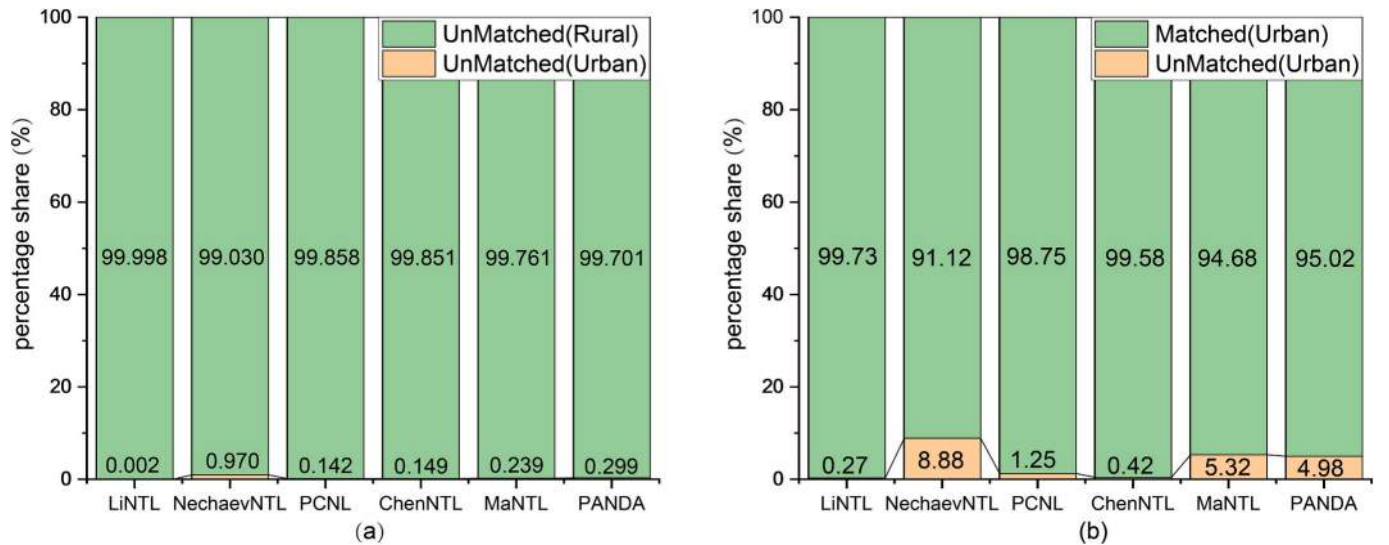


Fig. 20. Urban/rural comparison of the percentages of matched (including NN-M and SS-M) and unmatched (including SS-UM and SN-UM) units (Note: (a) urban/rural comparison of the un-matched units among ENTIL products; (b) comparison of the percentages of matched and unmatched units in urban areas among ENTIL products).

perform better in low-light environments. Additionally, DMSP/OLS products often encounter light saturation issues in urban areas, whereas products like VIIRS, designed with a high dynamic range, can more accurately reflect radiation characteristics in high-intensity urban light areas. Furthermore, variations in light source characteristics across different regions exacerbate the performance differences among NTL products. Urban areas have dense, concentrated light sources primarily from artificial sources, while rural areas are dominated by dispersed point sources. Thus, the performance of NTL products in different areas reflects the interplay between technical parameters and light intensity characteristics. This finding further suggests that when using ENTL products for long-term analysis of surface NTL emissions, researchers need to pay close attention to the specific characteristics of the study area to effectively reduce the risk of drawing biased conclusions due to data consistency limitations.

Besides, as shown in Fig. 21, we also selected four relatively representative nature reserves in Africa and South America that experienced various levels of light pollution. However, the recorded NTL intensity profiles based on the ENTL product showed that the light pollution intensity in the protected area had undergone a significant spike after 2012, and whether this was the real situation or caused by the consistency flaws in the data itself deserves more attention. Therefore, the precise time-series consistency quality layer for ENTL products can more clearly predict the dynamics of light pollution and human footprints,

greatly avoiding pseudo-conclusions due to flaws in data quality.

From the perspective of ENTL product users, our research provides valuable insights and actionable guidance for selecting the most suitable datasets based on consistency assessments. This is particularly relevant for urban planners, socio-economic researchers, and other practitioners who rely on nighttime light data for their analyses. Users should prioritize products with higher percentages of SS-Matched (SS-M) grid units, as these indicate a higher level of consistency and reliability across the full-period trends. For instance, globally oriented studies may benefit from using products like ChenNTL or NechaevNTL, which demonstrated superior consistency in our evaluations. Conversely, regional studies, such as those focused on China, might find PANDA particularly valuable due to its fine resolution and tailored calibration for local conditions. Moreover, users working in areas with high spatial heterogeneity, such as rural or low-light regions, should exercise caution with datasets showing higher proportions of SN-Unmatched (SN-UM) or SS-Unmatched (SS-UM) grid units, as these inconsistencies may affect analyses in these contexts. By aligning the choice of ENTL products with the findings from this study, users can mitigate uncertainties, enhance data reliability, and ensure their research outcomes are more robust and credible.

Despite the progress made, this study recognizes some limitations that should be clarified and attempted to be addressed in future work. Firstly, the hypothetical conditions for the constructed scheme in this

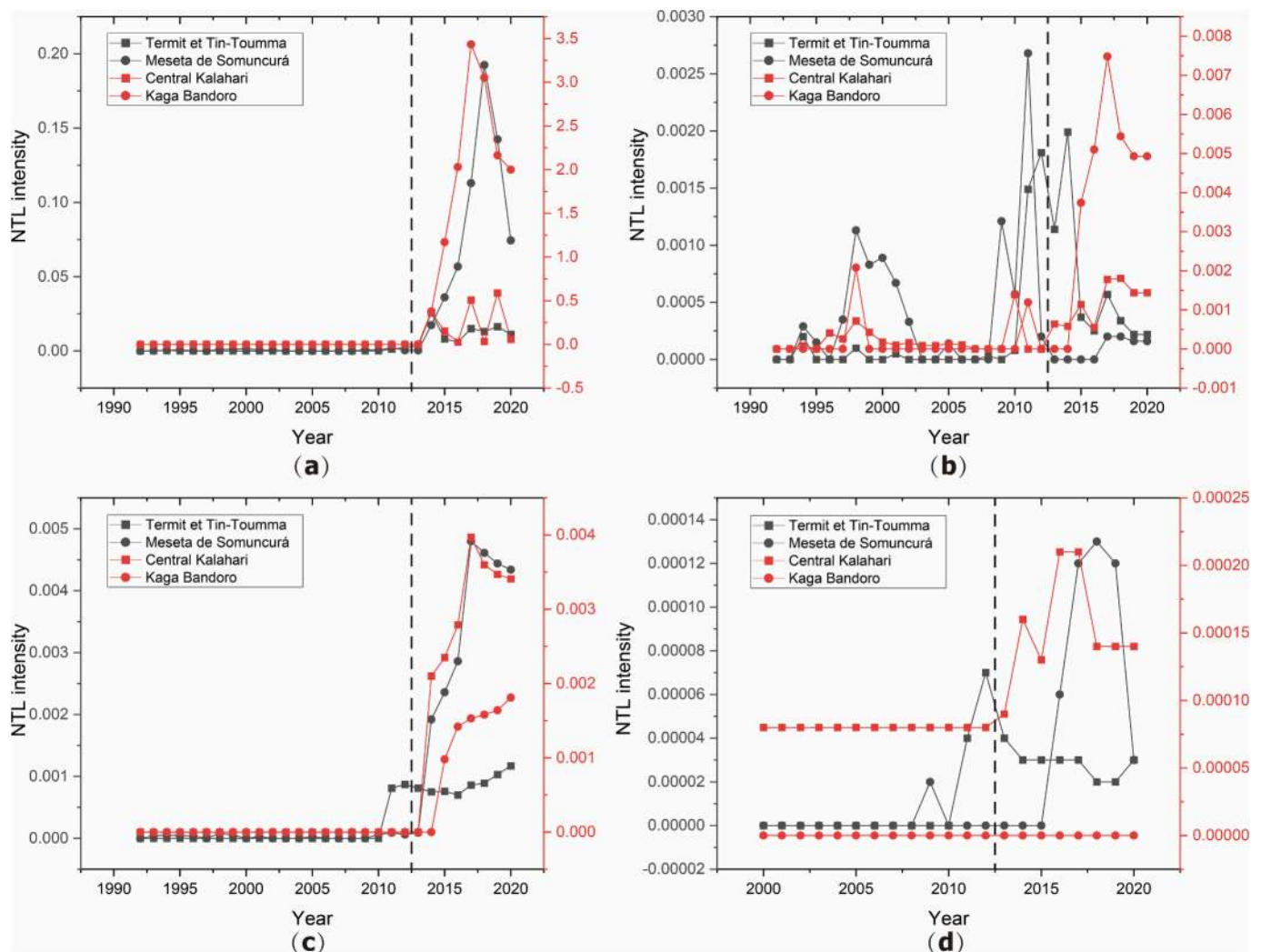


Fig. 21. Time-series NTL intensity dynamics profiles for four selected African protected areas based on different ENTL products (Note: (a) LiNTL; (b) NechaevNTL; (c) PCNL; (d) ChenNTL; and dotted line marks the starting year for cross-sensor calibration in ENTL products).

paper need to be better emphasized here. In constructing the logical combination rule, we hypothesized that the 2012 surface light emission intensities observed by OLS and VIIRS are identical, which is also the foundational assumption of almost all cross-sensor calibration models. However, since OLS and VIIRS have completely different transit times, with DMSP/OLS nighttime transit times typically ranging from 19:30 to 22:30 and NPP/VIIRS nighttime transit times being relatively constant at approximately 01:30, their recorded annual nighttime light intensities may trigger an intensity gap due to patterns of anthropogenic activity at night. In addition, the angular and seasonal effects of the VIIRS itself could be potential triggers for this gap (Wang et al., 2022; Li et al., 2025). Since this gap is embedded in almost all cross-sensor calibrated ENTL products, we believe this risk of bias arising in a consistency assessment based on the scheme developed in this paper is acceptable.

Besides, we adopted the most cautious strategy when designing the logic combinations and diagnostic rules, which resulted that significant trends and consistency quality levels could not be given for all grid cells globally in the SNID and LTIL layers. This limitation is due to the complexity and diversity of global NTL data, which may require more sophisticated analytical techniques to achieve full coverage. However, given that these units only account for a small part, we still believe that the proposed scheme is effective and feasible. In addition, while current consistency assessments have substantially improved the accuracy of ENTL products, further refinement of trend strength measurements could also enhance the granularity and utility of consistency assessments.

Certainly, there are still some limitations found in this study; for instance, the logical combinations and diagnostics designed in the implementation of SNID and LTIL still failed to give a definitive consistency assessment result for all grid units globally. However, given that these units only account for a small part, we still believe that the proposed scheme is effective and feasible. First, our scheme did not provide trend analysis and consistency assessment results for all grid units globally for prudential reasons. The enhancement of these aspects could provide more precise guidance for the selection and application of ENTL data, especially in critical areas sensitive to small changes in light emission.

6. Conclusion

Recently, the scheme of NTL time-series data consistency calibration (especially cross-sensor calibration) and ENTL products' continuous iteration have greatly contributed to the development of NTL remote sensing, and have been widely used in socio-economic and natural ecology-related applications at multiple scales. Compared to advances in ENTL products and data calibration, the methods and metrics used to assess the consistency quality with long time-series ENTL products have been relatively backward, limiting the accuracy and reliability of ENTL-based applications. Accordingly, this study developed a simple and efficient scheme for assessing consistency features at the unit scale based on dynamic trends and logical rules and selected several representative ENTL products for assessment and application based on this scheme. The results show:

- (1) The proposed ENTL products consistency quality assessment scheme based on logical combinations and diagnosis of temporal trends shows good indicativeness and robustness, and can efficiently and finely reveal the ENTL products consistency characteristics at the finer grid scale.
- (2) Based on this scheme, we produced a standard trend layer SNID for the period 1992–2020, which integrated multiple NTL products with good consistency and accuracy and can be used in other ENTL products consistency tests or light evolution-related studies.

- (3) The consistency quality assessment results of the six representative ENTL products revealed noticeable variations in their consistency characteristics, particularly in regions with high light intensity, rural areas, and high-latitude regions. These differences highlight the spatial heterogeneity in consistency levels among products, reflecting the influence of regional characteristics and calibration strategies.
- (4) We acknowledge the significant efforts made by previous researchers in the development of ENTL products, which have generally demonstrated good consistency and have been validated by numerous subsequent studies for their great potential and application value. However, we also recommend that users carefully select the most suitable ENTL products based on the scope of their study area, regional characteristics, and background information to enhance the precision and reliability of their research.

CRediT authorship contribution statement

Zihao Zheng: Writing – original draft, Visualization, Validation, Software, Methodology, Funding acquisition, Formal analysis, Data curation, Conceptualization. **Qiming Zheng:** Writing – review & editing, Software, Funding acquisition. **Zhifeng Wu:** Supervision, Investigation. **Zheng Cao:** Visualization, Validation. **Hong Zhu:** Funding acquisition. **Yingbiao Chen:** Software. **Benyan Jiang:** Methodology. **Yingfeng Guo:** Methodology. **Dong Xu:** Software. **Francesco Marinello:** Project administration, Data curation, Conceptualization.

Declaration of competing interest

The authors declare that they have no known competing financial interests or personal relationships that could have appeared to influence the work reported in this paper.

Data availability

Data will be made available on request.

Acknowledgements

This research was financially supported by the National Natural Science Foundation of China (No. 42430515, No. 42401432), Guangzhou Basic and Applied Basic Research Program (No. 2024A04J3666), Chinese University of Hong Kong (No. 4937239), General Research Fund of Research Grants Council of Hong Kong (No. 15204824). We would like to thank organizations that shared their datasets for use in this study. We would like to thank anonymous reviewers for their constructive comments and suggestions. The views and opinions expressed in this paper are those of the authors alone.

References

- Cao, C., Shao, X., Uprety, S., 2013. Detecting light outages after severe storms using the S-NPP/VIIRS day/night band radiances. *IEEE Geosci. Remote Sens. Lett.* 10 (6), 1582–1586.
- Cao, X., Wang, J., Chen, J., Shi, F., 2014. Spatialization of electricity consumption of China using saturation-corrected DMSP-OLS data. *Int. J. Appl. Earth Obs. Geoinf.* 28, 193–200.
- Chen, Z., Yu, B., Yang, C., Zhou, Y., Qian, X., Wang, C., Wu, J., 2020. An extended time-series (2000–2018) of global NPP-VIIRS-like nighttime light data from a cross-sensor calibration. *Earth Syst. Sci. Data Disc.* 2020, 1–34.
- Chen, H., Wu, B., Yu, B., Chen, Z., Wu, Q., Lian, T., Wu, J., 2021. A new method for building-level population estimation by integrating LiDAR, nighttime light, and POI data. *J. Remote Sensing*. 9803796.
- Chen, J., Gao, M., Cheng, S., Hou, W., Song, M., Liu, X., Liu, Y., 2022a. Global 1 km × 1 km gridded revised real gross domestic product and electricity consumption during 1992–2019 based on calibrated nighttime light data. *Scient. Data* 9 (1), 202.
- Chen, Z., Wei, Y., Shi, K., Zhao, Z., Wang, C., Wu, B., Yu, B., 2022b. The potential of nighttime light remote sensing data to evaluate the development of digital economy: a case study of China at the city level. *Comput. Environ. Urban. Syst.* 92, 101749.

- Claverie, M., Ju, J., Masek, J.G., Dungan, J.L., Vermote, E.F., Roger, J.C., Justice, C., 2018. The harmonized Landsat and Sentinel-2 surface reflectance data set. *Remote Sens. Environ.* 219, 145–161.
- Du, X., Shen, L., Wong, S.W., Meng, C., Yang, Z., 2021. Night-time light data based decoupling relationship analysis between economic growth and carbon emission in 289 Chinese cities. *Sustain. Cities Soc.* 73, 103119.
- Elvidge, C.D., Ziskin, D., Baugh, K.E., Tuttle, B.T., Ghosh, T., Pack, D.W., Zhizhin, M., 2009. A fifteen year record of global natural gas flaring derived from satellite data. *Energies* 2 (3), 595–622.
- Elvidge, C.D., Baugh, K., Zhizhin, M., Hsu, F.C., Ghosh, T., 2017. VIIRS night-time lights. *Int. J. Remote Sens.* 38 (21), 5860–5879.
- Elvidge, C.D., Hsu, F.C., Zhizhin, M., Ghosh, T., Taneja, J., Bazilian, M., 2020. Indicators of electric power instability from satellite observed nighttime lights. *Remote Sens. (Basel)* 12 (19), 3194.
- Elvidge, C.D., Zhizhin, M., Ghosh, T., Hsu, F.C., Taneja, J., 2021. Annual time series of global VIIRS nighttime lights derived from monthly averages: 2012 to 2019. *Remote Sens. (Basel)* 13 (5), 922.
- Ghosh, T., Elvidge, C.D., Hsu, F.C., Zhizhin, M., Bazilian, M., 2020. The dimming of lights in India during the COVID-19 pandemic. *Remote Sens. (Basel)* 12 (20), 3289.
- Ji, G., Tian, L., Zhao, J., Yue, Y., Wang, Z., 2019. Detecting spatiotemporal dynamics of PM_{2.5} emission data in China using DMSP-OLS nighttime stable light data. *J. Clean. Prod.* 209, 363–370.
- Jiang, W., Yuan, L., Wang, W., Cao, R., Zhang, Y., Shen, W., 2015. Spatio-temporal analysis of vegetation variation in the Yellow River Basin. *Ecol. Indic.* 51, 117–126.
- Jiang, W., He, G., Long, T., Wang, C., Ni, Y., Ma, R., 2017. Assessing light pollution in China based on nighttime light imagery. *Remote Sens. (Basel)* 9 (2), 135.
- Jiang, F., Chen, B., Li, P., Jiang, J., Zhang, Q., Wang, J., Deng, J., 2023. Spatio-temporal evolution and influencing factors of synergizing the reduction of pollution and carbon emissions-utilizing multi-source remote sensing data and GTWR model. *Environ. Res.* 229, 115775.
- Klomp, J., 2016. Economic development and natural disasters: a satellite data analysis. *Glob. Environ. Chang.* 36, 67–88.
- Levin, N., Kyba, C.C., Zhang, Q., de Miguel, A.S., Román, M.O., Li, X., Elvidge, C.D., 2020. Remote sensing of night lights: a review and an outlook for the future. *Remote Sens. Environ.* 237, 111443.
- Li, X., Zhou, Y., 2017. A stepwise calibration of global DMSP/OLS stable nighttime light data (1992–2013). *Remote Sens. (Basel)* 9 (6), 637.
- Li, X., Chen, X., Zhao, Y., Xu, J., Chen, F., Li, H., 2013. Automatic intercalibration of night-time light imagery using robust regression. *Remote Sens. Lett.* 4 (1), 45–54.
- Li, R., Liu, X., Li, X., 2015. Estimation of the PM_{2.5} pollution levels in Beijing based on nighttime light data from the defense meteorological satellite program-operational linescan system. *Atmosphere* 6 (5), 607–622.
- Li, X., Li, D., Xu, H., Wu, C., 2017. Intercalibration between DMSP/OLS and VIIRS night-time light images to evaluate city light dynamics of Syria's major human settlement during Syrian Civil War. *Int. J. Remote Sens.* 38 (21), 5934–5951.
- Li, S., Sun, D., Goldberg, M.D., Sjöberg, B., Santek, D., Hoffman, J.P., Holloway, E., 2018a. Automatic near real-time flood detection using Suomi-NPP/VIIRS data. *Remote Sens. Environ.* 204, 672–689.
- Li, X., Liu, S., Jendryke, M., Li, D., Wu, C., 2018b. Night-time light dynamics during the Iraqi civil war. *Remote Sens. (Basel)* 10 (6), 858.
- Li, X., Zhan, C., Tao, J., Li, L., 2018c. Long-term monitoring of the impacts of disaster on human activity using DMSP/OLS nighttime light data: a case study of the 2008 Wenchuan, China Earthquake. *Remote Sensing* 10 (4), 588.
- Li, X., Zhao, L., Li, D., Xu, H., 2018d. Mapping urban extent using Luojia 1-01 nighttime light imagery. *Sensors* 18 (11), 3665.
- Li, X., Zhou, Y., Zhao, M., Zhao, X., 2020. A harmonized global nighttime light dataset 1992–2018. *Scient. Data* 7 (1), 168.
- Li, Y., Ye, H., Gao, X., Sun, D., Li, Z., Zhang, N., Zheng, J., 2021. Spatiotemporal patterns of urbanization in the three most developed urban agglomerations in China based on continuous nighttime light data (2000–2018). *Remote Sens. (Basel)* 13 (12), 2245.
- Li, S., Cao, X., Zhao, C., Jie, N., Liu, L., Chen, X., Cui, X., 2023. Developing a pixel-scale corrected nighttime light dataset (PCNL, 1992–2021) combining DMSP-OLS and NPP-VIIRS. *Remote Sens. (Basel)* 15 (16), 3925.
- Li, J., Li, X., Li, D., 2025. Impact of vegetation phenology on anisotropy of artificial light at night-evidence from multi-angle satellite observations. *Remote Sens. Environ.* 317, 114525.
- Liang, L., Bian, J., Li, A., Feng, W., Lei, G., Zhang, Z., Zuo, J., 2020. Consistent intercalibration of nighttime light data between DMSP/OLS and NPP/VIIRS in the China–Pakistan Economic Corridor. *J. Remote Sensing* 24 (2), 149–160.
- Ma, J., Guo, J., Ahmad, S., Li, Z., Hong, J., 2020. Constructing a new inter-calibration method for DMSP-OLS and NPP-VIIRS nighttime light. *Remote Sens. (Basel)* 12 (6), 937.
- Mammides, C., 2020. A global assessment of the human pressure on the world's lakes. *Glob. Environ. Chang.* 63, 102084.
- Mandanici, E., Bitelli, G., 2016. Preliminary comparison of Sentinel-2 and Landsat 8 imagery for a combined use. *Remote Sens. (Basel)* 8 (12), 1014.
- Mu, H., Li, X., Wen, Y., Huang, J., Du, P., Su, W., Geng, M., 2022. A global record of annual terrestrial Human Footprint dataset from 2000 to 2018. *Scient. Data* 9 (1), 176.
- Narayanan, P., Sarkar, S., Basistha, A., Sachdeva, K., 2016. Trend analysis and forecast of pre-monsoon rainfall over India. *Weather* 71 (4), 94–99.
- Nechaev, D., Zhizhin, M., Poyda, A., Ghosh, T., Hsu, F.C., Elvidge, C., 2021. Cross-sensor nighttime lights image calibration for DMSP/OLS and SNPP/VIIRS with residual U-net. *Remote Sens. (Basel)* 13 (24), 5026.
- Panwar, M., Agarwal, A., Devadas, V., 2018. Analyzing land surface temperature trends using non-parametric approach: a case of Delhi, India. *Urban Clim.* 24, 19–25.
- Román, M.O., Wang, Z., Sun, Q., Kalb, V., Miller, S.D., Molthan, A., Masuoka, E.J., 2018. NASA's Black Marble nighttime lights product suite. *Remote Sens. Environ.* 210, 113–143.
- Román, M.O., Stokes, E.C., Shrestha, R., Wang, Z., Schultz, L., Carlo, E.A.S., Enenkel, M., 2019. Satellite-based assessment of electricity restoration efforts in Puerto Rico after Hurricane Maria. *PLoS One* 14 (6), e0218883.
- Shi, K., Yang, Q., Fang, G., Yu, B., Chen, Z., Yang, C., Wu, J., 2019. Evaluating spatiotemporal patterns of urban electricity consumption within different spatial boundaries: a case study of Chongqing, China. *Energy* 167, 641–653.
- Shi, K., Wu, Y., Li, D., Li, X., 2022. Population, GDP, and carbon emissions as revealed by SNPP-VIIRS nighttime light data in China with different scales. *IEEE Geosci. Remote Sens. Lett.* 19, 1–5.
- Shi, K., Yu, B., Ma, J., Cao, W., Cui, Y., 2023. Impacts of slope climbing of urban expansion on global sustainable development. *The Innovation* 4 (6), 100529.
- Stokes, E.C., Seto, K.C., 2019. Characterizing urban infrastructural transitions for the sustainable development goals using multi-temporal land, population, and nighttime light data. *Remote Sens. Environ.* 234, 111430.
- Wang, Z., Román, M.O., Sun, Q., Molthan, A.L., Schultz, L.A., Kalb, V.L., 2018. Monitoring disaster-related power outages using NASA black marble nighttime light product. *Int. Arch. Photogramm. Remote Sens. Spat. Inf. Sci.* 42, 1853–1856.
- Wang, J., Roudini, S., Hyer, E.J., Xu, X., Zhou, M., Garcia, L.C., Da Silva, A.M., 2020. Detecting nighttime fire combustion phase by hybrid application of visible and infrared radiation from Suomi NPP VIIRS. *Remote Sens. Environ.* 237, 111466.
- Wang, Z., Shrestha, R.M., Román, M.O., Kalb, V.L., 2022. NASA's black marble multiangle nighttime lights temporal composites. *IEEE Geosci. Remote Sens. Lett.* 19, 1–5.
- Wu, K., Wang, X., 2019. Aligning pixel values of DMSP and VIIRS nighttime light images to evaluate urban dynamics. *Remote Sens. (Basel)* 11 (12), 1463.
- Wu, J., He, S., Peng, J., Li, W., Zhong, X., 2013. Intercalibration of DMSP-OLS night-time light data by the invariant region method. *Int. J. Remote Sensing* 34 (20), 7356–7368.
- Xu, P., Wang, Q., Jin, J., Jin, P., 2019. An increase in nighttime light detected for protected areas in mainland China based on VIIRS DNB data. *Ecol. Indic.* 107, 105615.
- Xu, D., Yang, F., Yu, L., Zhou, Y., Li, H., Ma, J., Cheng, J., 2021. Quantization of the coupling mechanism between eco-environmental quality and urbanization from multisource remote sensing data. *J. Clean. Prod.* 321, 128948.
- Xu, J., Wang, J., Li, R., Yang, X., 2023. Spatio-temporal effects of urbanization on CO₂ emissions: evidence from 268 Chinese cities. *Energy Policy* 177, 113569.
- Yang, Z., Chen, Y., Guo, G., Zheng, Z., Wu, Z., 2021. Using nighttime light data to identify the structure of polycentric cities and evaluate urban centers. *Sci. Total Environ.* 780, 146586.
- Yin, R., He, G., Jiang, W., Peng, Y., Zhang, Z., Li, M., Gong, C., 2021. Night-time light imagery reveals China's city activity during the COVID-19 pandemic period in early 2020. *IEEE J. Select. Topics Appl. Earth Observ. Remote Sensing* 14, 5111–5122.
- Yu, B., Lian, T., Huang, Y., Yao, S., Ye, X., Chen, Z., Wu, J., 2019. Integration of nighttime light remote sensing images and taxi GPS tracking data for population surface enhancement. *Int. J. Geogr. Inf. Sci.* 33 (4), 687–706.
- Yu, B., Wang, C., Gong, W., Chen, Z., Shi, K., Wu, B., Hong, Y., Li, Q., Wu, J., 2021. Nighttime light remote sensing and urban studies: data , methods , applications, and prospects. *Natl Remote Sensing Bull.* 25 (1), 342–364.
- Zhang, Q., Seto, K.C., 2011. Mapping urbanization dynamics at regional and global scales using multi-temporal DMSP/OLS nighttime light data. *Remote Sens. Environ.* 115 (9), 2320–2329.
- Zhang, Q., Pandey, B., Seto, K.C., 2016. A robust method to generate a consistent time series from DMSP/OLS nighttime light data. *IEEE Trans. Geosci. Remote Sens.* 54 (10), 5821–5831.
- Zhang, L., Ren, Z., Chen, B., Gong, P., Xu, B., Fu, H., 2024. A prolonged artificial nighttime-light dataset of China (1984–2020). *Scient. Data* 11 (1), 414.
- Zhao, X., Yu, B., Liu, Y., Yao, S., Lian, T., Chen, L., Wu, J., 2018. NPP-VIIRS DNB daily data in natural disaster assessment: evidence from selected case studies. *Remote Sens. (Basel)* 10 (10), 1526.
- Zhao, M., Zhou, Y., Li, X., Cao, W., He, C., Yu, B., Zhou, C., 2019. Applications of satellite remote sensing of nighttime light observations: advances, challenges, and perspectives. *Remote Sens. (Basel)* 11 (17), 1971.
- Zhao, M., Zhou, Y., Li, X., Cheng, W., Zhou, C., Ma, T., Huang, K., 2020. Mapping urban dynamics (1992–2018) in Southeast Asia using consistent nighttime light data from DMSP and VIIRS. *Remote Sens. Environ.* 248, 111980.
- Zhao, C., Cao, X., Chen, X., Cui, X., 2022. A consistent and corrected nighttime light dataset (CCNL 1992–2013) from DMSP-OLS data. *Scient. Data* 9 (1), 424.
- Zheng, Q., Weng, Q., Wang, K., 2019a. Developing a new cross-sensor calibration model for DMSP-OLS and Suomi-NPP VIIRS night-light imagery. *ISPRS J. Photogramm. Remote Sens.* 153, 36–47.
- Zheng, Z., Yang, Z., Chen, Y., Wu, Z., Marinello, F., 2019b. The interannual calibration and global nighttime light fluctuation assessment based on pixel-level linear regression analysis. *Remote Sens. (Basel)* 11 (18), 2185.
- Zheng, Q., Weng, Q., Wang, K., 2021a. Characterizing urban land changes of 30 global megacities using nighttime light time series stacks. *ISPRS J. Photogramm. Remote Sens.* 173, 10–23.
- Zheng, Z., Wu, Z., Chen, Y., Guo, G., Cao, Z., Yang, Z., Marinello, F., 2021b. Africa's protected areas are brightening at night: a long-term light pollution monitor based on nighttime light imagery. *Glob. Environ. Chang.* 69, 102318.

- Zheng, Z., Wu, Z., Cao, Z., Zhang, Q., Chen, Y., Guo, G., Marinello, F., 2022. Estimates of power shortages and affected populations during the initial period of the Ukrainian-Russian conflict. *Remote Sens. (Basel)* 14 (19), 4793.
- Zheng, Q., Seto, K.C., Zhou, Y., You, S., Weng, Q., 2023. Nighttime light remote sensing for urban applications: progress, challenges, and prospects. *ISPRS J. Photogramm. Remote Sens.* 202, 125–141.
- Zhou, M., Wang, J., Chen, X., Xu, X., Colarco, P.R., Miller, S.D., Holben, B., 2021. Nighttime smoke aerosol optical depth over US rural areas: first retrieval from VIIRS moonlight observations. *Remote Sens. Environ.* 267, 112717.